University of Stavanger

Faculty of Science and Technology

MASTER'S THESIS

Study program/Specialization: Petroleum Geosciences Engineering	Spring, 2015 Open
Writer: David Thor Odinsson	_____ (Writer's signature)
Faculty supervisor: Nestor Cardozo External supervisor(s): Lothar Schulte	
Title of thesis: Influence of seismic and velocity uncertainties on reservoir volumetrics	
Credits (ECTS): 30	
Keywords: Uncertainty Geostatistics Volume attributes Experimental design	Pages: 80 Stavanger, 15th June, 2015

Influence of seismic and velocity uncertainties on reservoir volumetrics

by

David Thor Odinsson, B.Sc.

Thesis

Presented to the Faculty of Science and Technology

The University of Stavanger

The University of Stavanger

June 2015

Acknowledgements

This thesis report has been carried out at the department of petroleum engineering at the University of Stavanger, Norway under the supervision of Nestor Cardozo and Lothar Schulte.

I would like to acknowledge the University of Stavanger for providing the workspace for the duration of this study.

I would like to thank Nestor Cardozo for reviewing my work and providing me with helpful comments.

I express my sincere gratitude to Lothar Schulte for his dedication, countless hours of inspirational discussions and providing helpful comments to accomplish this study.

Finally, I would like to thank my family for their love and support during my two years of study at the University of Stavanger.

Abstract

Influence of seismic and velocity uncertainties on reservoir volumetrics

David Thor Odinsson, M.Sc.

The University of Stavanger, 2015

Supervisor: Nestor Cardozo; Lothar Schulte

Uncertainty is a well-known concept in geology, and can lead to re-evaluation of important development decisions if properly assessed. This thesis describes uncertainty through the set-up of "scenarios". For each parameter used for the structural model a so-called low case, base case and high case are defined. The combination of the different cases results in many structural models that deliver a distribution of the bulk volume. A generally acknowledged way of handling the large number of models coming from the different combinations of the model parameters is experimental design.

This study has shown that the uncertainty in the seismic picks and consequently in the reservoir thickness have a large impact on the gross-volume. The reservoir structural geometry controls the influence of fault uncertainty on the reservoir volume. Well velocities used in this thesis for domain conversion are quite accurate but sparsely sampled and therefore subject to uncertainty. In addition, the

geologic complexity may have a dramatic influence on the uncertainty of the depth conversion.

A proper assessment of seismic and velocity uncertainties can be applied to risk analysis for field appraisal and development, hydrocarbon volume estimation, accurate well placement, optimal well trajectory and reservoir history matching.

Table of Contents

List of Tables ix

List of Figures x

1. Introduction 1

2. Data 8

3. Methodology 10

3.1 Well data 10

3.2 Capturing uncertainty in seismic interpretation 14

3.2.1 Horizons 14

3.2.2 Faults 18

3.2.3 Volume attributes 19

3.3 Depth conversion based on well data 21

3.4 Structural modeling 24

3.5 Experimental Design 25

4. Observations 30

4.1 Synthetic Seismogram observation 30

4.2 Seismic Interpretation and uncertainty estimation 32

4.21. Horizons 32

4.2.2 Faults 42

4.3 Depth conversion 45

4.3.1 Linear velocity law 45

4.3.2 Blind well test for estimating uncertainty in depth 47

4.4 Uncertainty in gross-volume derived from modelled structural uncertainty 51

4.4.1 Numerical 3-D reservoir model 58

5. Discussion 61

5.1 Uncertainty in stratigraphic horizons 61

5.2 Uncertainty in fault position 62

5.3 Uncertainty in depth conversion 63

5.4 Experimental design 63

6. Conclusion 65

References.....66

List of Tables

Table 1. Well information. 8

Table 2. Experimental design matrix. 26

Table 3. Time error statistics. 40

Table 4. Depth error statistics. 50

Table 5. Combinations and volume results of structural models for the Placket-Burman experimental design. 51

Table 6. Combinations and volume results of structural models for the full factorial experimental design 53

Table 7. Explanation of the parameters and coefficients in the 25 term volume equation. 56

Table 8. Random experimental run and its corresponding numerical 3-D model. 58

List of Figures

Figure 1. Stochastic simulation of geological surfaces using P-field simulation. ...4
Figure 2. Fault constructed from horizon fault lines.....5
Figure 3. Geological constraints on faults. 7
Figure 4. Depth structure map outlining the area of interest. 9
Figure 5. Sand and shale distribution in four wells. 10
Figure 6. Convolution model of a synthetic trace.....12
Figure 7. Well-15, seismic well tie. 13
Figure 8. High, base and low case of top reservoir.....15
Figure 9. High, base and low case reservoir time thickness for base case top reservoir surface.....16
Figure 10. Reservoir time thickness uncertainty.....16
Figure 11. Experimental variogram. 17
Figure 12. Fault uncertainty envelope. 18
Figure 13. Fault slicing. 19
Figure 14. Original seismic vs. Structural smoothing.....19
Figure 15. Original seismic vs. Cosine of instantaneous phase. 20
Figure 16. Ant track workflow.....21
Figure 17. Two linear velocity functions. 22
Figure 18. Depth surface adjusted to wells. 23
Figure 19. Time thickness map converted to depth. 24
Figure 20. Base reservoir depth surface constructed from depth thickness map...24
Figure 21. Structural modeling. 25
Figure 22. Synthetic seismogram from Well-15.....30
Figure 23. Synthetic seismogram from well-15, well-14 and well-13. 31
Figure 24. Time structure map of top reservoir. 32

Figure 25. Section A. 33
Figure 26. Section A, frame 1. 34
Figure 27. Section A, frame 2. 34
Figure 28. Section B. 35
Figure 29. Section B, frame 1. 35
Figure 30. Section B, frame 2. 35
Figure 31. Section B, frame 3. 36
Figure 32. Section C. 36
Figure 33. Section C, frame 1. 37
Figure 34. Section C, frame 2. 37
Figure 35. Time error distribution due to statics. 38
Figure 36. Seismic intersections showing offset wells. 39
Figure 37. Time error distribution of the top reservoir. 40
Figure 38. Time error distribution of the reservoir thickness. 40
Figure 39. Variogram analysis of time errors for top reservoir. 41
Figure 40. Variogram analysis of the reservoir thickness in the time domain. 41
Figure 41. Section A. 42
Figure 42. Time slices from ant track volume. 43
Figure 43. Fault slicing of the northern fault. 44
Figure 44. Linear velocity law vs. checkshot interval velocities from Well-1 and Well-15. 45
Figure 45. Problems in depth conversion.. 46
Figure 46. Difference map of the two depth surfaces using Convergent Interpolation and Moving Average. 47
Figure 47. Depth structure map of top reservoir. 48
Figure 48. Depth error distribution of the top reservoir based on the blind well test. 48

Figure 49. Variogram analysis of depth errors. 49
Figure 50. Thickness depth error distribution in the depth domain. 50
Figure 51. Variogram analysis of depth thickness errors. 50
Figure 52. Placket-Burman experimental design. a) Observed volume vs. Predicted volume. b) Residual plot. 52
Figure 53. Influence of parameters on the base case volume. 53
Figure 54. Full factorial experimental design 25 terms. a) Observed volume vs. Predicted volume. b) Residual plot. 55
Figure 55. Full factorial experimental design 25 terms. a) Observed volume vs. Predicted volume. b) Residual plot 57
Figure 56. a) Volume distribution for 5000 calculations of the volume equation. b) Cumulative density function of the volume distribution. 58
Figure 57. Fault parameter values scaled to the interval [0,1]. 59
Figure 58. Full factorial experimental design for 25 terms. a) Observed volume vs. predicted volume, numerical model indicated with red circle. b) Residual plot. 60

1. Introduction

Success in the oil and gas exploration and production (E&P) industry relies on accurate positioning and interpretation of geological structures, as well as the use of decision analysis. A proper assessment of seismic and velocity uncertainties can be applied to risk analysis for field appraisal and development, accurate well placement, optimal well trajectory, reservoir history matching and gross-rock volume estimation (Vincent et.al., 1999; Thore et al., 2002 and Osypov et.al., 2011).

Experiments of uncertainties related to subsurface structures require a geoscientist to create 3-D structural models. Structural models integrate different types of data, e.g. 3-D/2-D seismic reflection surveys, borehole information, field observations and analog models, each subject to different types of uncertainty. Data most used for creating 3-D structural models of the subsurface are seismic images obtained through seismic reflection surveys (Caers, 2011). Seismic reflection Surveys follow the principles of seismology by generating artificial seismic waves and measuring the time it takes the waves to travel from its source to a receiver on the surface. Compiling and processing the travel time measurements results in an image of the subsurface. Seismic images are a useful tool in creating three-dimensional models but they are subject to inherent uncertainties, which directly affect the input data for the structural model.

In a geologic context, uncertainty and error is easily confused. Uncertainty is the recognition that our results may deviate from reality, whereas error expresses the quantified uncertainty (Bárdossy *et al.*, 2001). Mann (1993) studied uncertainty in geology and classified uncertainties into three different types and listed possible

sources for each type. According to Mann (1993), Type I uncertainties refer to error, bias and imprecision in the data. Type II uncertainties refer to stochasticity, for example due to inhomogeneity and anisotropy in rock units. Type III uncertainties refer to lack of knowledge or a need for generalization, predicting future or past events for instance. Uncertainties of type I and II are quantitative and can be handled by statistical methods, while uncertainties of type III are qualitative and theoretically unknowable (Mann, 1993).

This thesis describes uncertainty through the set-up of "scenarios". For each parameter used for the structural model a so-called low case, base case and high case are defined. The combination of the different cases results in many structural models that deliver a distribution of the bulk volume. This distribution represents the bulk volume uncertainty of the reservoir. A generally acknowledged way of handling the large number of models coming from the different combinations of the model parameters is experimental design. Experimental design is based on multiple linear regression techniques to derive a volume equation capable of predicting the reservoir volume for any combination of the model parameters.

The study area for this thesis is in the Gulf of Mexico. This region started to form in the Middle to Late Triassic (230 Ma) as a result of intracontinental rifting between the Yucatan and North America (Bird *et al.,* 2005). According to Galloway (2008), marine transgression into the continental area during the Middle Jurassic resulted in the formation of extensive salt deposits. Tectonic activity during the Late Cretaceous – Early Paleogene provided large quantities of terrigenous siliciclastic sediments from uplifted source areas. This continued sediment influx resulted in the accumulation of a wedge of Cenozoic deposits. These progradational deposits contain

reservoir, source, and seal units and are characterized by alternating sand reservoirs and thick sealing shales. In addition, there are large growth faults and rollover anticlines associated with tectonics, sedimentation and salt movement (Bascle *et al.*, 2001).

Many authors have contributed different techniques and methods for estimating and quantifying uncertainty. For example, Thore *et al*., (2002) divided the steps involved in the construction of a structural model into six phases: acquisition, preprocessing, stacking, migration, interpretation and time-to-depth conversion and discussed sources of uncertainty related to each phase. Their method to generate multiple realizations of the structural model involves using a stochastic approach with the algorithm of probability field simulation. This algorithm samples a local conditional probability distribution that covers a range of possible outcomes of the simulated variable, while forcing neighboring probability values to have some similarities (Srivastava, 1992). First, a randomly selected value from the conditional cumulative distribution function corresponding to a local probability value is added to the base case surface (Figure 1). The local probability is correlated to the neighboring nodes with a variogram describing the lateral correlation of the surface. In addition, Thore *et al.,* (2002) used a vertical variogram for intercorrelation between horizons. Finally, the simulation is performed using any geostatistical methods that can reproduce spatial correlation.

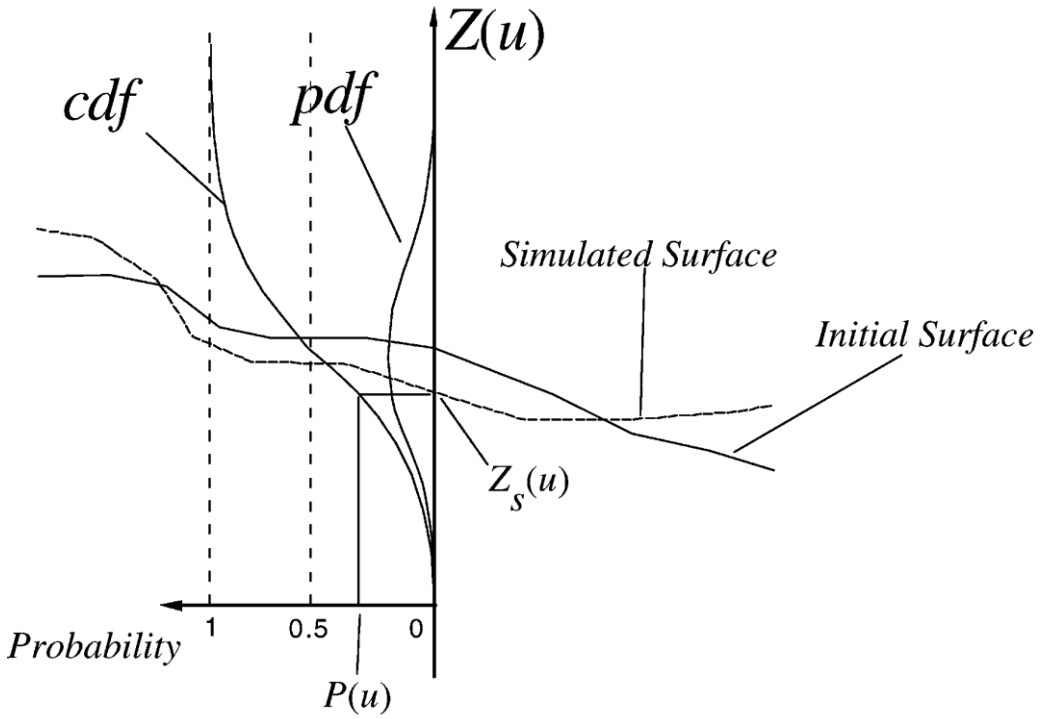

Figure 1. Stochastic simulation of geological surfaces using P-field simulation (Thore et al., 2002).

Samson *et al.,* (1996) studied uncertainties related to stratigraphic horizons through computing gross volume by stacking thickness maps of lithological units below the top reservoir. In this way, they separated the uncertainty of the overburden and the uncertainty of the reservoir units.

Faults are generally assumed as two-dimensional objects represented by surfaces, "even though they are three-dimensional zones of deformation" (Røe *et al.*, 2014). This inevitably leads to uncertainty in their position and initial geometry when digitizing them for instance, as "fault sticks" on seismic sections. Lecour *et al.,* (2001) applied a stochastic approach for fault modeling. Their method involves constructing the faults by calculating the intersection of the horizons with the envelope of the fault zone (horizons lines). These horizon limits are linearly interpolated within the fault zone and the fault plane defined by the median line given by the mid points of the

interpolated lines (Figure 2). Their simulation methods involve the application of probability field simulation controlled by a random function generator.

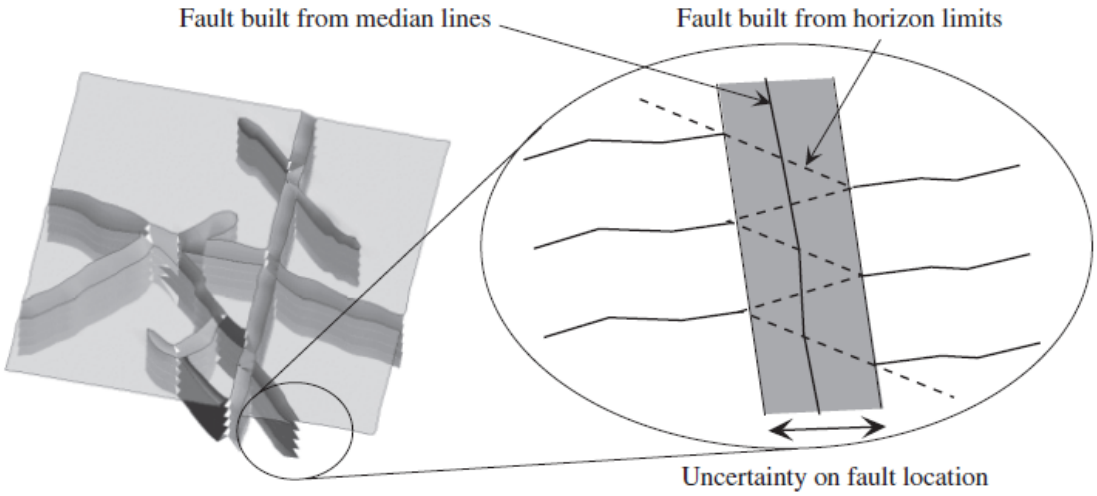

Figure 2. Fault constructed from horizon fault lines (Lecour et.al, 2001).

Velocity information is required for the time-to-depth conversion. Such information can be derived from processing, i.e. seismic velocities or from well measurements (Thore *et al.*, 2002). Check-shot surveys and vertical seismic profiles provide a highly accurate time-depth relationship. However, this velocity information is limited to the borehole location and does not capture lateral variations (Hart, 2011). Thore *et al.*, (2002) applied cross validation technique by using the blind well test for measuring the velocity uncertainties. However, the blind well test only delivers reliable results for a large number of wells in the study area.

Following the division of Thore *et al.*, (2002) for the steps involved in the construction of a structural model, this thesis addresses uncertainties related to interpretation and depth conversion. The analysis of the errors coming from acquisition and processing are beyond the scope of this study.

Seismic uncertainties involve parameterizing and quantifying the uncertainty of the reservoir location and the geometry of faults from interpreted seismic data in the time domain. The structural uncertainty analysis of the reservoir model includes the quantification of the uncertainty coming from the seismic interpretation in the time domain. The reservoir under consideration consists of a top and a base horizon captured by the seismic interpretation. Both horizons share a common source of uncertainty coming from the overburden. This error includes static problems and migration uncertainties of the seismic. The base reservoir horizon includes an additional uncertainty coming from the reservoir thickness. The method outlined by Samson *et al.*, (1996), is applied so that the top reservoir horizon reflects the uncertainty in the location of the reservoir, while the reservoir base is generated by stacking thickness maps of lithological units below the top reservoir.

Fault geometries are constrained by basic geological rules explained in figure 3: they should not display inversion of curvature along the vertical axis and retain a high wavelength of sinuosity along the horizontal axis for the reservoir interval (Lecour *et al.*, 2001). In addition, faults should retain their dip direction along the horizontal axis.

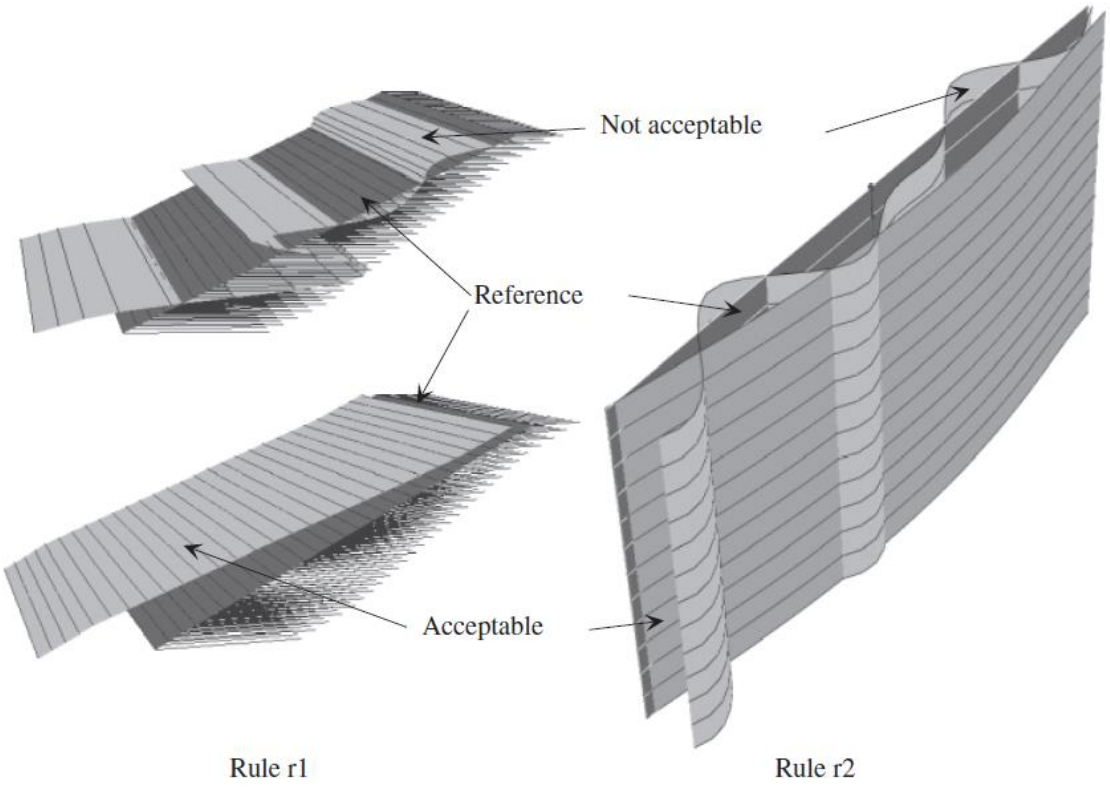

Figure 3. Geological constraints on faults (Lecour, et.al, 2001).

Another major source for structural uncertainty is depth conversion. The blind well test is an important tool to determine the velocity uncertainties and derive a depth error distribution, representative for the whole area under investigation outside the influence radius of the wells.

This thesis will differentiate itself from previous research in using experimental design for describing the structural uncertainty analytically and capturing the gross volume uncertainty of the reservoir through several thousand runs of the volume equation with stochastically selected model parameter values. Finally, a novel method is discussed that provides the possibility to set up a numerical 3-D reservoir model for a parameter set used by any of the runs of the volume equation.

2. Data

The research area is covered by a 16.7 km^2 of 3-D reflection seismic survey consisting of 270 cross-lines and 220 in-lines with fifty-five feet spacing. The trace length ranges from 0-3500 milliseconds (ms) with processing performed at four ms sample interval. There are twenty-seven wells, of which twenty-five are inside the research area with well log information. Table 1 shows the available well logs used in this study for each well through the reservoir interval. Also available for these wells are densely sampled check shot surveys that give accurate average velocity measurements. The top and the base of the reservoir are defined by well tops and can be identified by seismic events.

Table 1. Well information.

Well name	Reservoir interval							
	MD-Top (ft)	MD-Base (ft)	TWT-Top (ms)	TWT-Base (ms)	Gamma	Density	Neutron	Sonic
Well-1	6162.00	6241.00	1778.21	1797.22	X	X	X	-
Well-2	6130.00	6209.00	1779.70	1798.73	-	-	-	X
Well-3	6433.00	6548.00	1858.52	1885.78	-	-	-	X
Well-4	6468.00	6577.00	1802.97	1826.14	X	-	X	X
Well-5	5846.00	5912.00	1723.99	1740.16	-	-	-	X
Well-6	6427.00	6514.00	1818.04	1837.73	X	-	-	X
Well-7	6412.00	6528.00	1834.53	1860.78	-	-	-	X
Well-8	6536.00	6650.00	1860.31	1885.83	-	-	-	X
Well-9	-	-	-	-	X	-	-	X
Well-10	6536.00	6650.00	1834.26	1859.54	-	-	-	X
Well-11	6299.00	6435.00	1824.57	1856.97	-	-	-	X
Well-12	6413.00	6522.00	1839.92	1864.44	-	-	-	X
Well-13	6365.00	6502.00	1855.90	1888.48	X	X	-	X
Well-14	6663.00	6805.46	1910.04	1943.83	-	X	-	X
Well-15	6376.00	6498.00	1842.50	1871.34	X	X	X	X
Well-16	6227.00	6317.00	1796.14	1816.55	-	-	-	X
Well-17	6208.00	6298.00	1804.90	1826.23	-	-	-	X
Well-18	6593.00	6657.00	1629.82	1642.67	-	-	-	X
Well-19	5370.00	5405.00	1613.03	1621.96	-	-	-	X
Well-20	6237.00	6285.00	1751.76	1762.95	X	-	-	X
Well-21	6678.00	6804.00	1832.29	1859.81	-	-	-	X

Well-22	6386.00	6493.00	1820.33	1844.76	-	-	-	X
Well-23	6474.00	6601.00	1868.65	1898.93	-	-	-	X
Well-24	6418.00	-	1792.80	-	-	-	-	X
Well-25	6387.59	6444.54	1812.00	1824.94	-	-	-	X
Well-26	6179.00	6269.00	1797.15	1818.70	X	-	-	X
Well-27	Outside	Outside	Outside	Outside	Outside	Outside	Outside	Outside
Well-28	Outside	Outside	Outside	Outside	Outside	Outside	Outside	Outside

The area of interest for the development of the methodology for this uncertainty study consists of two horizons, top and base reservoir, and is bounded by two east-west striking normal faults (Figure 4). The reservoir volume is calculated above the oil water contact. The data in this study shows a salt dome in the western edge of the seismic volume, outside the analyzed reservoir. The poor data quality near the salt would have made an interpretation a challenge, given the time constraints.

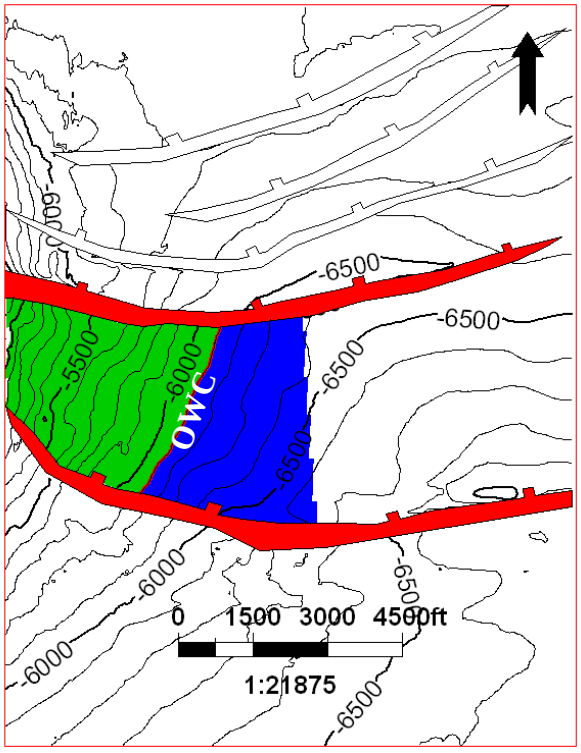

Figure 4. Depth structure map outlining the area of interest.

3. Methodology

This chapter discusses data calibration, uncertainty quantification, the steps involved in creating structural models, and the method used to derive a distribution for the gross volume of the reservoir.

3.1 WELL DATA

The reservoir under consideration shows characteristics of alternating shale and sand bodies covered by a shale layer (Figure 5). The shale is characterized by high GR (gamma-ray), RHOB (density) and NPHI (neutron porosity) values. The sand shows low GR, RHOB and NPHI values. Using the cross-over display of RHOB and NPHI, using a reverse scale for NPHI, allows to identify the sand bodies as shown by Well-1 in figure 5. Based on the well log interpretation, the well tops were defined for the top and base boundaries of the reservoir.

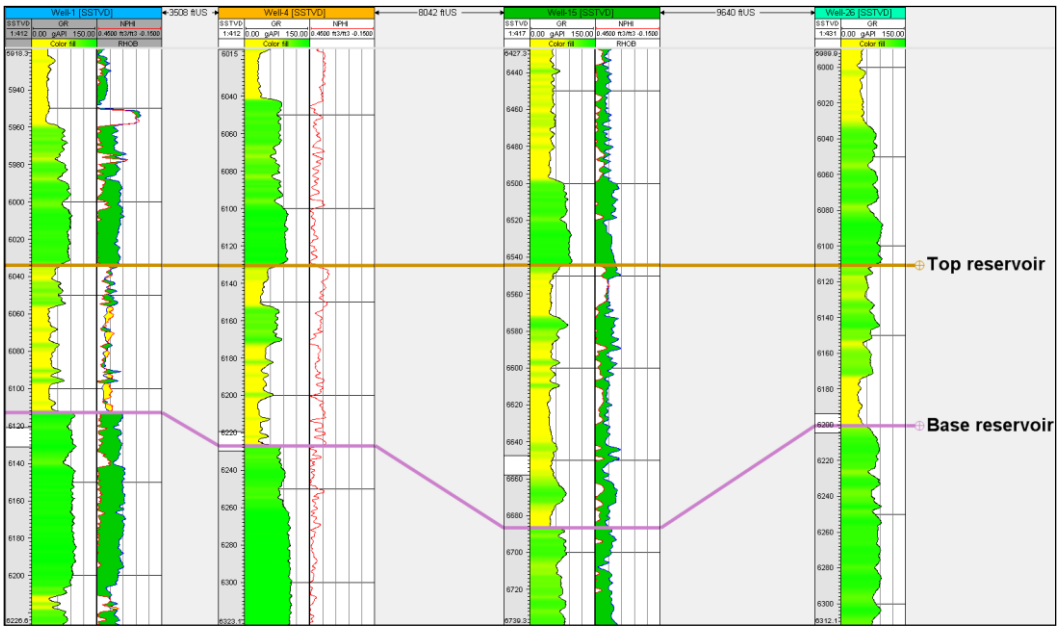

Figure 5. Sand and shale distribution in four wells. First track shows gamma ray log, second track shows neutron and density logs.

The seismic is based on changes in the acoustic impedance, which typically occur at lithological boundaries. The sonic log measures velocity on a frequency range much higher than the seismic and typically starts several meters below datum (Schlumberger, 2009). A checkshot survey provides more accurate seismic velocity information at each checkshot point than the sonic log and allows for a better comparison of the well data with the seismic. However, check shot surveys with large check shot spacing can provide inaccurate time-depth information between the check shot points. By calibrating the sonic log with a checkshot survey, a more accurate time-depth relationship at the wells is derived. The principle of sonic calibration involves fitting a drift curve to the check shot points (Schlumberger, 2009). First, the drift curve is obtained by subtracting the integrated sonic times from the check shot times. The resultant drift points are interpolated usually with a polynomial function. Finally, the drift curve is added to the integrated sonic time, which is finally converted to the calibrated sonic log. The final step establishes a link between the seismic and the wells through generating a synthetic seismogram. The steps involved in calculating the synthetic trace are shown in Figure 6. The sonic log (D_t) and density log (ρ) are converted into the time domain with the help of the check shot survey. The acoustic impedance log (AI) is derived from the sonic and the density log as:

$$\mathrm{AI} = \rho * \frac{1}{D_t} \qquad (3.1)$$

The reflectivity (RF) is derived from the acoustic impedance log:

$$RF_i = \frac{(\mathrm{AI_{i+1}} - \mathrm{AI_i})}{(\mathrm{AI_i} + \mathrm{AI_{i+1}})} \qquad (3.2)$$

$$i: number\ of\ sample$$

Finally, the reflectivity is convolved with a wavelet, which results in the synthetic trace.

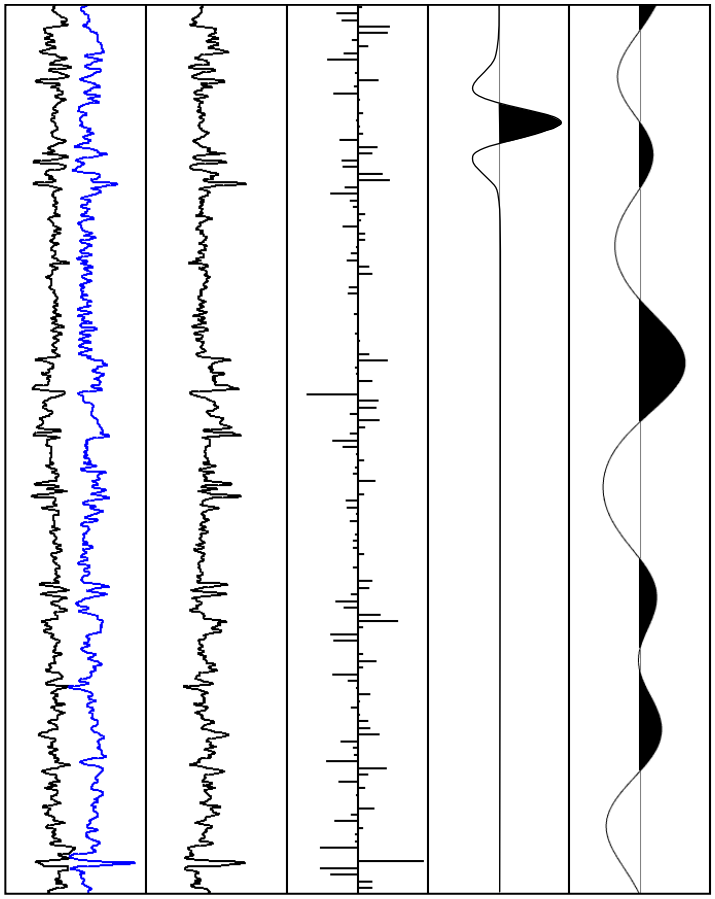

Figure 6. Convolution model of a synthetic trace. First track shows density (blue) and sonic (black), second track shows derived acoustic impedance, third track shows calculated reflectivity, fourth track shows Ricker wavelet, fifth track shows synthetic seismog

The match between the synthetic trace and the seismic depends highly on the wavelet. Often a so-called Ricker-wavelet with a user-defined mid-frequency is used. Figure 7 shows the seismic well tie for Well-15. In the left-most track it shows the sonic log (black) and the density log (blue). In the next track the reflectivity is shown. It is convolved with the displayed Ricker wavelet, which delivers the synthetic trace displayed in the middle of the seismic section, which is closest to the well location. The last track (to the right) shows the correlation between the synthetic trace and the

seismic trace closest to the well position. The vertical axis is the "lag" axis. A horizontal dashed white line marks the zero lag position. The match between the synthetic and the seismic is done through adjusting the center frequency of the wavelet. The maximum correlation, shown by a white asterix, should be at zero lag, which means there is no shift between the synthetic and the seismic. In case of non-zero lag, a constant shift needs to be applied to the synthetic in order to get a good match with the seismic event. Finally, the time-depth relationship needs to be updated to consider the final constant shift. The sign of the maximum correlation defines the polarity of the seismic. A positive maximum correlation indicates SEG polarity; a negative maximum correlation indicates European polarity.

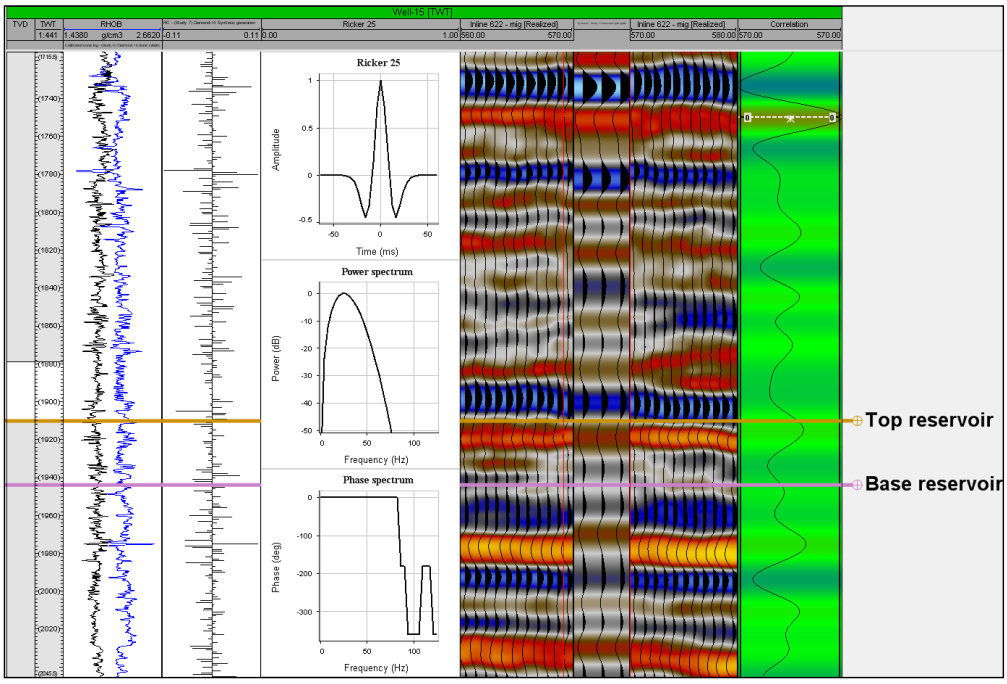

Figure 7. Well-15, seismic well tie.

3.2 CAPTURING UNCERTAINTY IN SEISMIC INTERPRETATION

This study is based on the key assumption that well tops are correct even though in reality there is uncertainty associated with well top determinations. A major source of this uncertainty lies in the difficulty of correlating the events interpreted on a well with the neighboring wells. Uncertainty coming from seismic interpretation is captured by three interpretation versions reflecting the high case, base case and low case. The high case results in a bulk volume increase and the low case in a bulk volume decrease with respect to a reference case (base case).

3.2.1 HORIZONS

Making a reliable seismic well tie prior to the interpretation phase ensures that the correct seismic event is being picked. Manual picking is required in areas of a low signal-to-noise ratio where the seismic event is distorted (high uncertainty). Auto tracking is automatically picking the seismic event through comparing the amplitudes and cross correlation of neighboring traces within a small time-window (L. Schulte, personal communication, March 25, 2015). It can be applied in areas of a coherent seismic event. Auto tracking is a very efficient way of picking a horizon and delivers a reproducible interpretation. 3-D guided auto tracking creates a dense interpretation following the seismic event minimizing the need for manual interpretation. Applying 3-D seismic attributes that enhance the continuity of reflectors, such as structural smoothing or cosine of instantaneous phase, assists in manually picking in areas of high uncertainty (see section 3.2.3).

Typically, well tops do not accurately match the seismic event. They may correspond to a different phase on the seismic image or show a small offset.

Measuring this time offset between the interpreted horizon and the well tops delivers a two-way-time (TWT) error distribution. Only if the error distribution shows a non-zero mean is the top reservoir surface shifted accordingly to acquire a Gaussian distribution of the time errors. The standard deviation of this error distribution is used to construct the high and low case horizons for the top reservoir. All horizons (low, base and high case) are adjusted to the well tops (Figure 8).

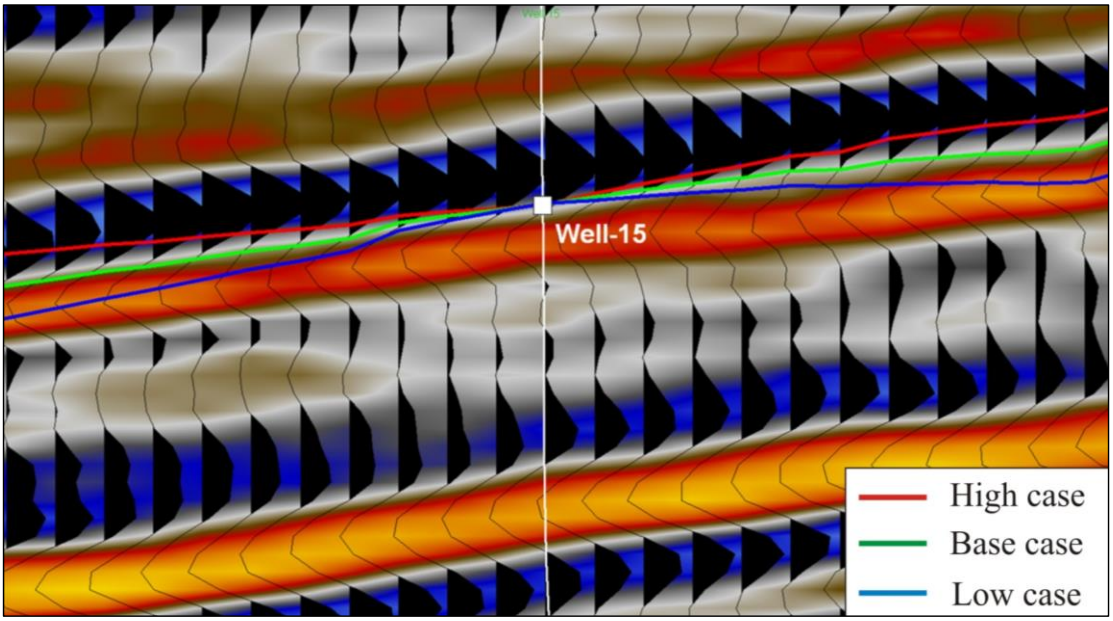

Figure 8. High, base and low case of the top reservoir.

Constructing the low and high case for the reservoir base involves stacking thickness maps below the top reservoir (Figure 9). The base case of the reservoir thickness is derived from the tracked top and base horizons that are not adjusted to the well tops. This thickness map is stacked below the top horizon that has been adjusted to the well tops (Figure 10). Measuring the TWT error between the constructed reservoir base and the well tops delivers the thickness uncertainty. The standard

deviation of the thickness error is used to construct the low and high case of the thickness maps.

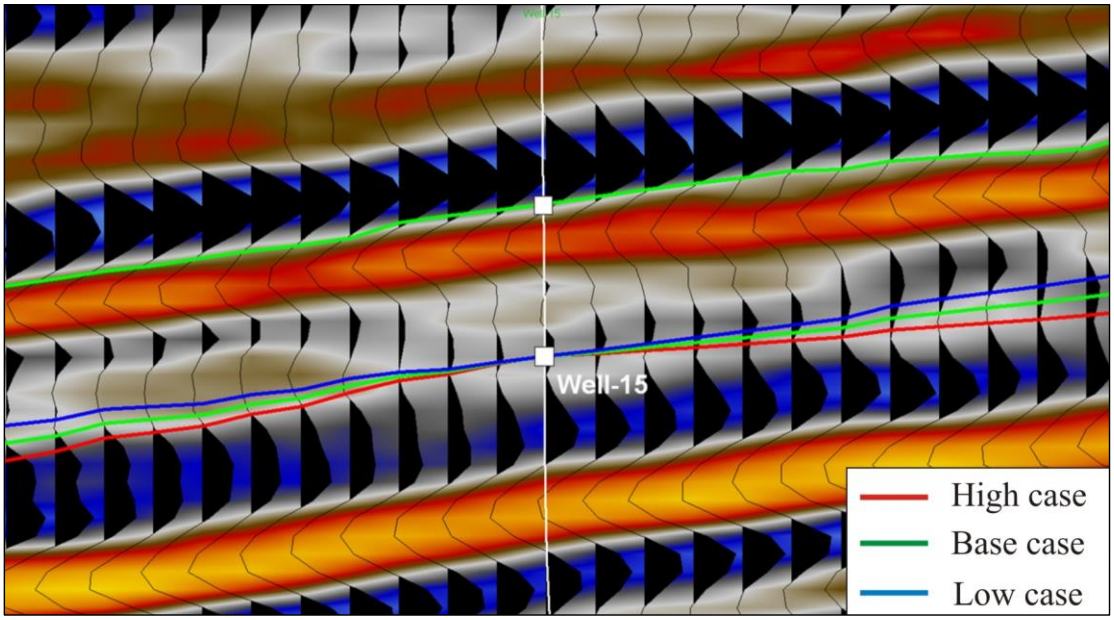

Figure 9. High, base and low case reservoir time thickness for base case top reservoir surface.

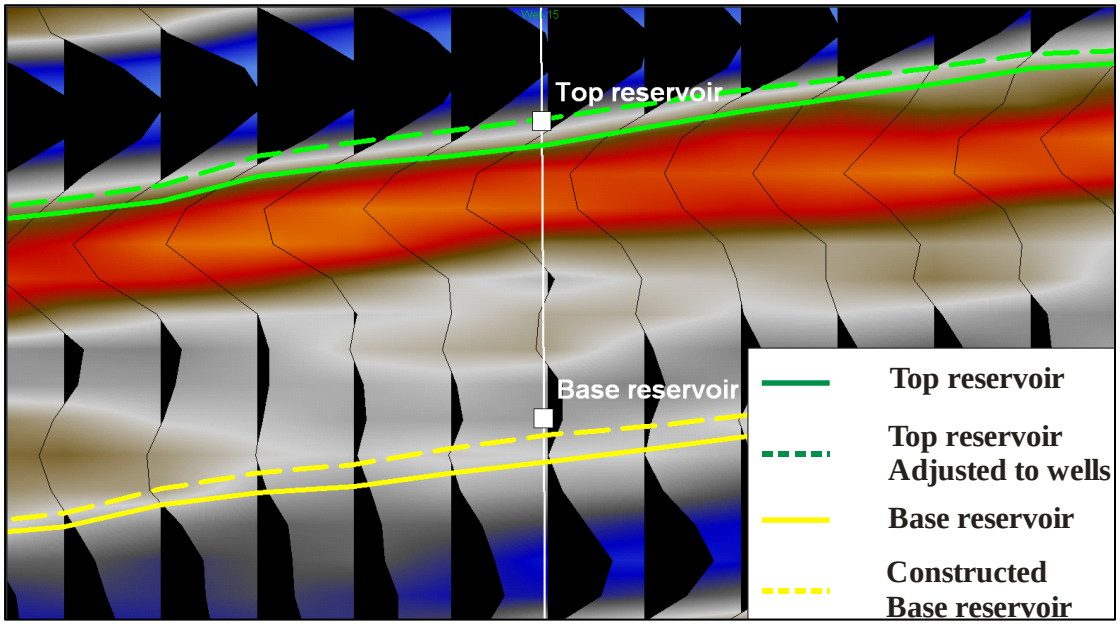

Figure 10. Reservoir time thickness uncertainty.

Variogram analysis of the time errors is used to determine the influence radius of the wells used for the well top adjustment. The principles of deriving the variogram

function involves collecting point pairs separated by a so called “lag distance” to describe the natural variation in the data in a specified direction (Caers, 2005). The squared difference between all point pairs are gathered for a single value of variance for a certain lag distance and repeated for different lag distances. An experimental variogram plots these variance points against the corresponding lag distance, shown as red circles in figure 11. A model variogram, represented by a spherical, Gaussian or exponential function is fitted to the experimental variogram, shown by the black curve in figure 11, where the data points of the experimental variogram appear to flatten horizontally. Variance points that plot above the sill of the model variogram are said to display no statistical similarities and the corresponding range is the spatial correlation of the data in a specified direction (Caers, 2005). The variogram model is needed by kriging or Gaussian simulation. For this study, the range of the variogram model is used as input to the Petrel mapping algorithm that flexes the time and depth surfaces to the well tops.

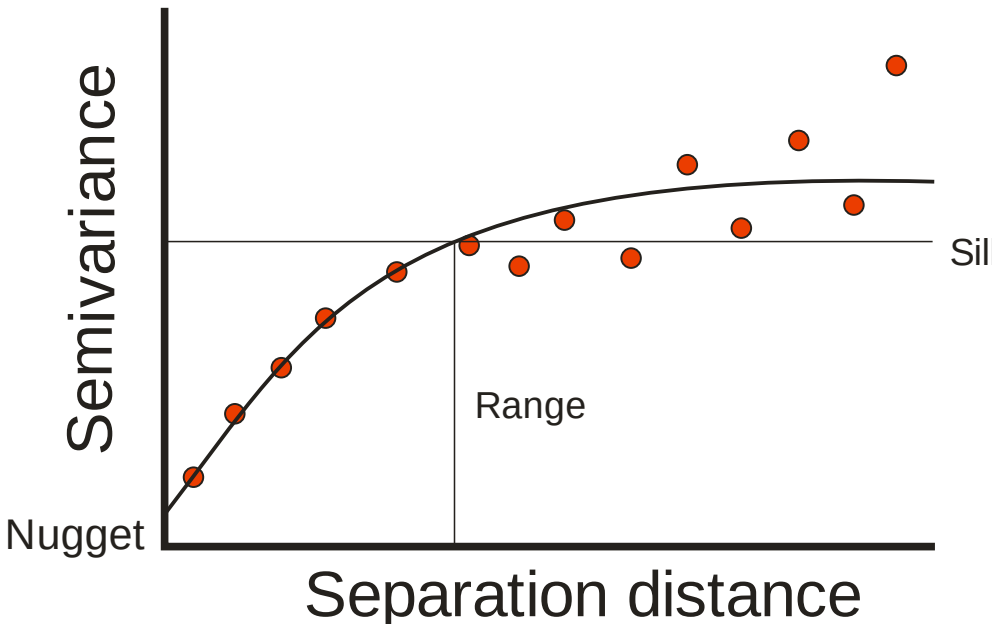

Figure 11. Experimental variogram.

3.2.2 FAULTS

In seismic faults are characterized by amplitude variations, changes in reflectors dip or reflector discontinuities/offsets. The 3-D seismic attributes that measure these characteristics can be a powerful tool for fault detection. The ant track workflow (see section 3.2.3) results in a volume that highlights the deformation zone around the faults and provides the possibility of drawing polygons outlining the fault envelope. The envelope represents the uncertainty in the fault interpretation that approximates the 3D fault zone by a fault plane. All polygons drawn on several time slices are gathered forming a couple of hanging wall – footwall sets for each fault describing the high and low case. A median line is computed and linked to each set to create the base case fault (Figure 12). This method ensures that the median line is nearly centered on the ant tracked event.

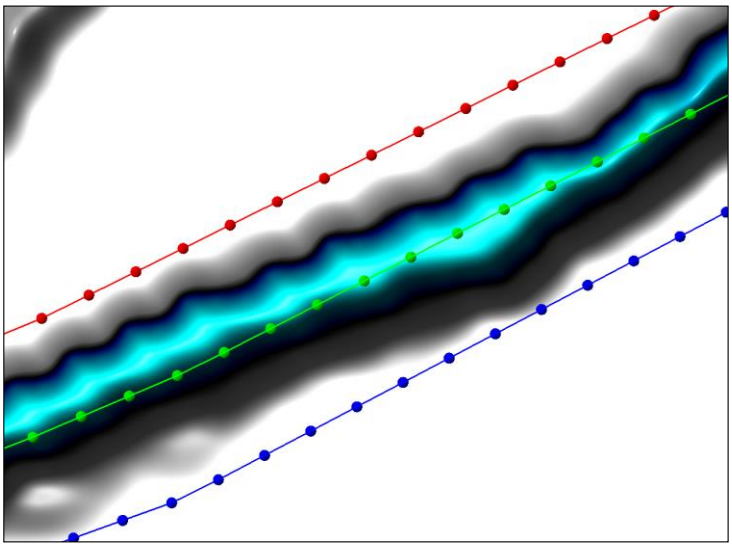

Figure 12. Fault uncertainty envelope. Median line (green) calculated between high case (red) and low case (blue).

Fault slicing provides a way to quality check the assumed width of the fault envelope by projecting the ant track volume onto the base case fault plane. The fault

plane is translated by a certain user-defined distance into the hanging wall and footwall. This process is called fault slicing and allows observing amplitude changes (Figure 13) at the edges of the fault zones that are characterized by the onset of the high amplitudes.

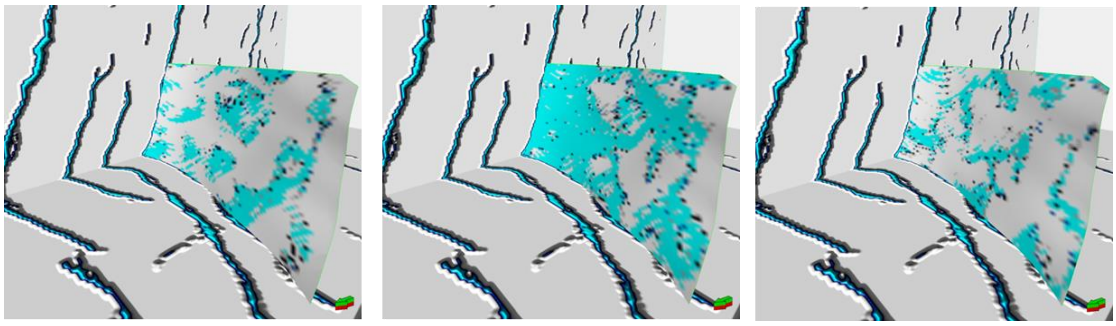

Figure 13. Fault slicing. Ant track volume projected onto the base case fault surface (middle) showing amplitude changes with a step-out distance of 100 feet into the hanging wall (left) and footwall (right).

3.2.3 VOLUME ATTRIBUTES

Structural smoothing performs data smoothing of the input signal by applying Gaussian weighted average filtering following the trend of the seismic events after determining the local dip and azimuth of the structure (Schlumberger, 2010). This attribute increases the signal-to-noise ratio, which can be useful for structural interpretation (Figure 14).

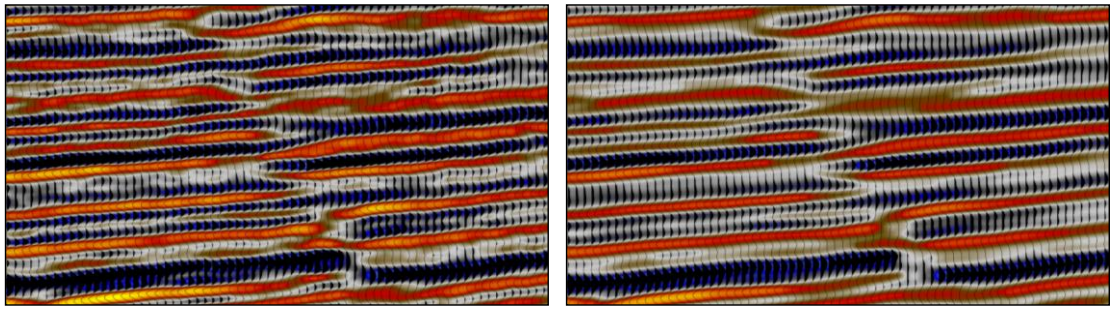

Figure 14. Original seismic (left) vs. Structural smoothing (right).

Cosine of instantaneous phase as the name suggests is the cosine function of the instantaneous phase angle φ(t). Mathematically, the instantaneous phase is given by:

$$\varphi(t) = \tan^{-1}[(g(t)/f(t))] \quad (3.3)$$

f(t) is the real part of the complex seismic signal and g(t) its imaginary part (Schlumberger, 2010). This attribute is linked to the instantaneous phase and therefore not sensitive to amplitude variations (L. Schulte, personal communication, March 25, 2015). The peak of the cosine of instantaneous phase is at the position of the seismic amplitude peaks, its troughs located at the seismic amplitude troughs. Therefore, it is possible to track a seismic horizon on this attribute. Often in noisy or complex areas, it is easier to interpret on the cosine of instantaneous phase than on the original seismic cube because of its amplitude-independent character. Figure 15 shows the same section of the original seismic and of the cosine of instantaneous phase cube. Obviously, it is easier to follow the seismic events on the attribute cube because the amplitude dependence is gone.

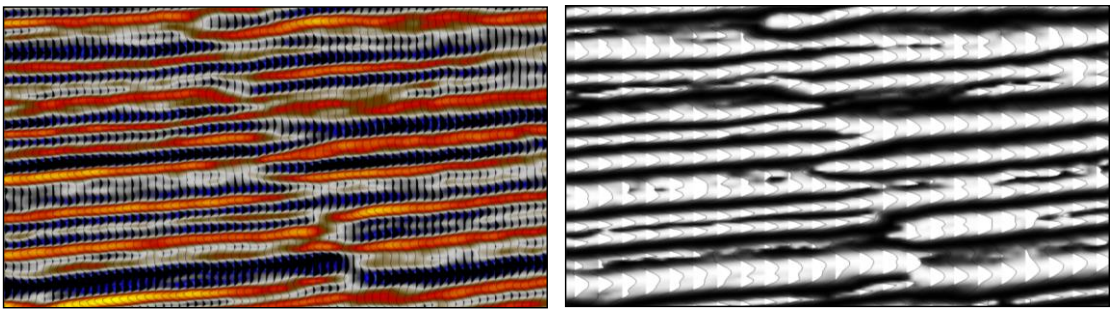

Figure 15. Original seismic (left) vs. Cosine of instantaneous phase (right).

Ant tracking uses the principles of swarm intelligence to extract events shown by high amplitudes in a preconditioned seismic cube (Figure 16). Typically the

attribute processes chaos or variance are applied to the seismic cube. Both attributes highlight the discontinuities in the seismic signal and hence are optimum for fault detection. Ant tracking deploys agents (ants) on the preconditioned volume. Each ant agent searches for local maxima and tries to follow these events (faults). The parameter control allows the user to apply constraints to the ant agents, which defines the number of tracked faults and the quality (coherent noise) of the ant track volume (Schlumberger, 2010).

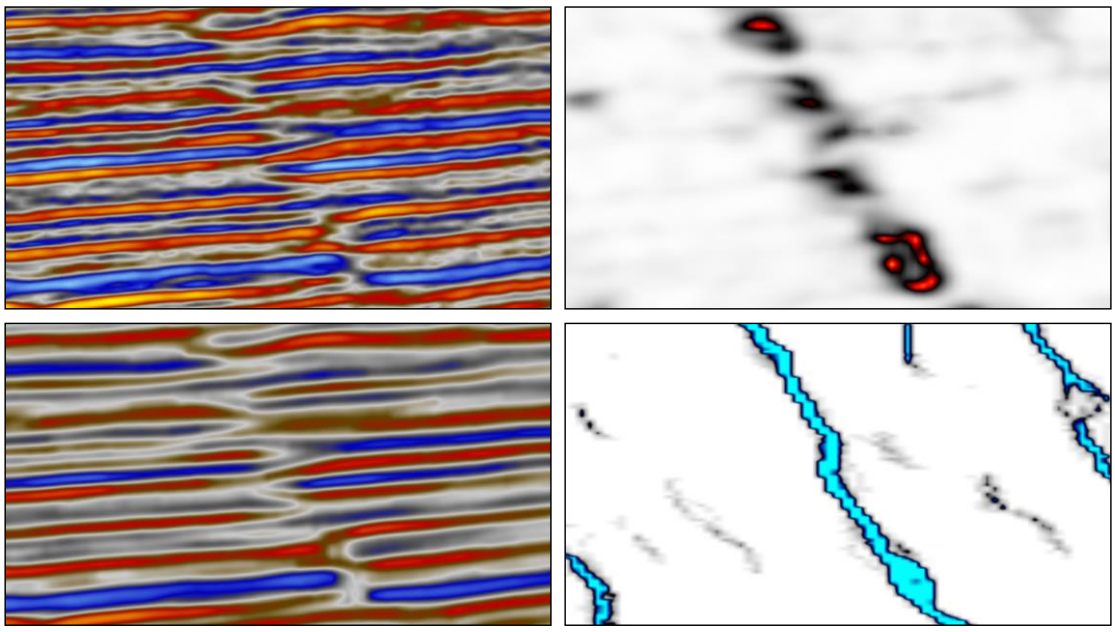

Figure 16. Ant track workflow. Original seismic (top left), Structural smoothing (bottom left), variance (top right) and ant track (bottom right).

3.3 DEPTH CONVERSION BASED ON WELL DATA

The interpretation is done in the time domain, but the volume calculation must be done in the depth domain. Therefore, time-to-depth conversion is necessary. Using the linear velocity law in a layer cake model down to the top of the reservoir should take into account major velocity boundaries of the overburden layers to get a more accurate depth of the top reservoir. The velocity model process (Petrel) offers two

types of linear velocity functions (Figure 17). Both functions give the same result at the wells, but derive the V_0 at different locations. K is the slope of the linear velocity law and describes the increase in velocity with depth. Therefore, K is related to compaction. The K value of the velocity law for each layer is the average of the k value derived at each well for the layer under consideration. It is kept constant since compaction is considered as a regional event. As this project deals with a thin reservoir interval velocities are used to depth convert the reservoir time thickness. The calculation of the interval velocities is based on the well top depths and the surface times at the well top positions.

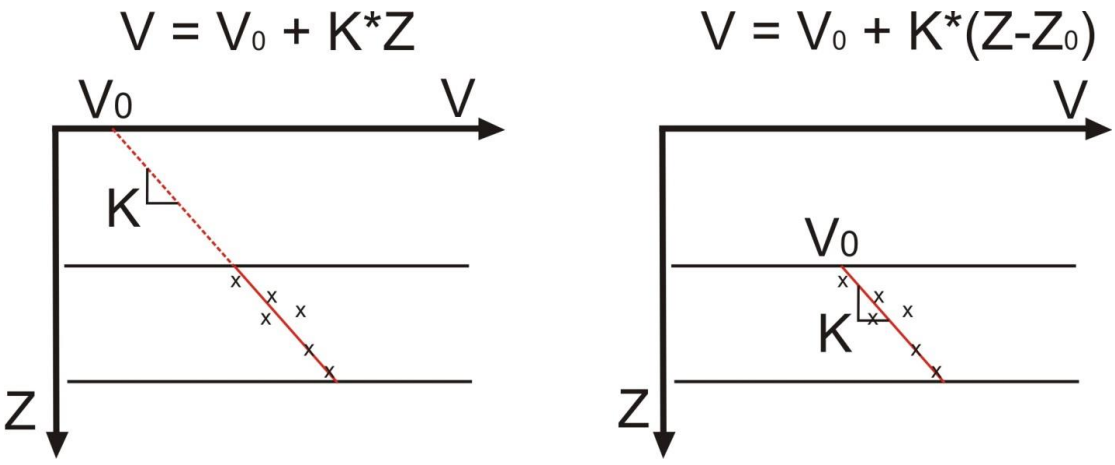

Figure 17. Two linear velocity functions (Schlumberger, Petrel manual, Velocity modeling course, 2009) (edited by author).

The depth error of the top reservoir coming from the velocity uncertainty is estimated with a blind well test. The velocity model is set up based on all wells with the exception of one well. The difference between the depth surface and the well top depth of the left out well is measured. This process is repeated for all wells to get a distribution of the depth errors. The assumption is that this error distribution describes the depth uncertainty at any location of the depth surface outside the radius of

influence of the wells. In practical terms, this means that the depth error of the surface at the position of a new well lies within the depth error distribution derived by the blind well test. The depth error standard deviation is used to derive the low and high case of the depth surface describing the top reservoir.

The estimation of the depth error of the reservoir base is done in two steps. First, the depth surface of the reservoir top is adjusted to the well tops (Figure 18). Second, the depth uncertainty of the reservoir base is estimated by applying a constant interval velocity to the reservoir time layer (L. Schulte, personal communication, March 25, 2015) (Figure 19). The constant velocity is estimated through averaging the interval velocities derived at all wells. The depth thickness resulting from the constant interval velocity is stacked below the reservoir top giving the reservoir base (Figure 20). The well tops at the reservoir base deliver the depth error distribution describing the uncertainty of the reservoir base surface.

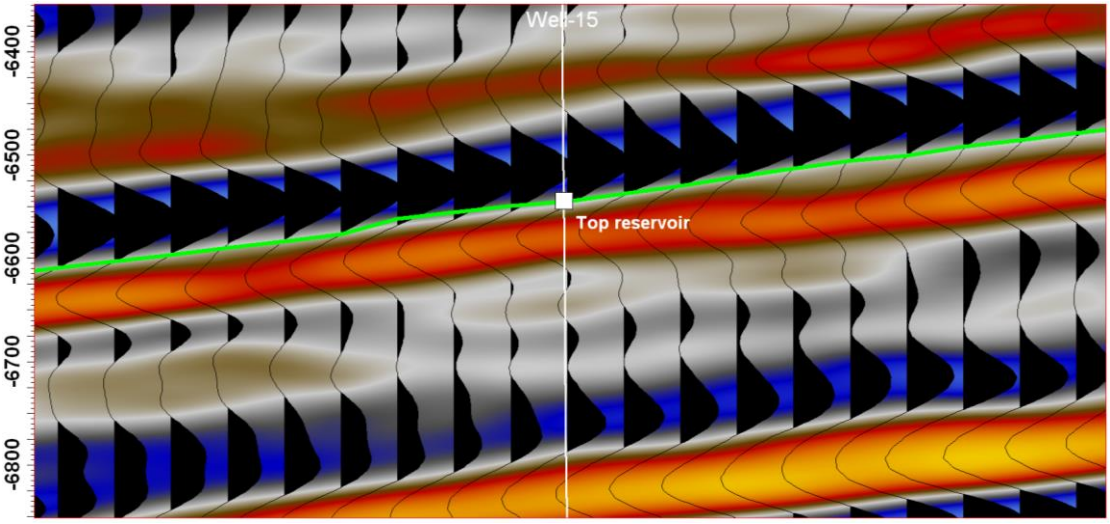

Figure 18. Depth surface adjusted to wells. Intersect given in figure 19.

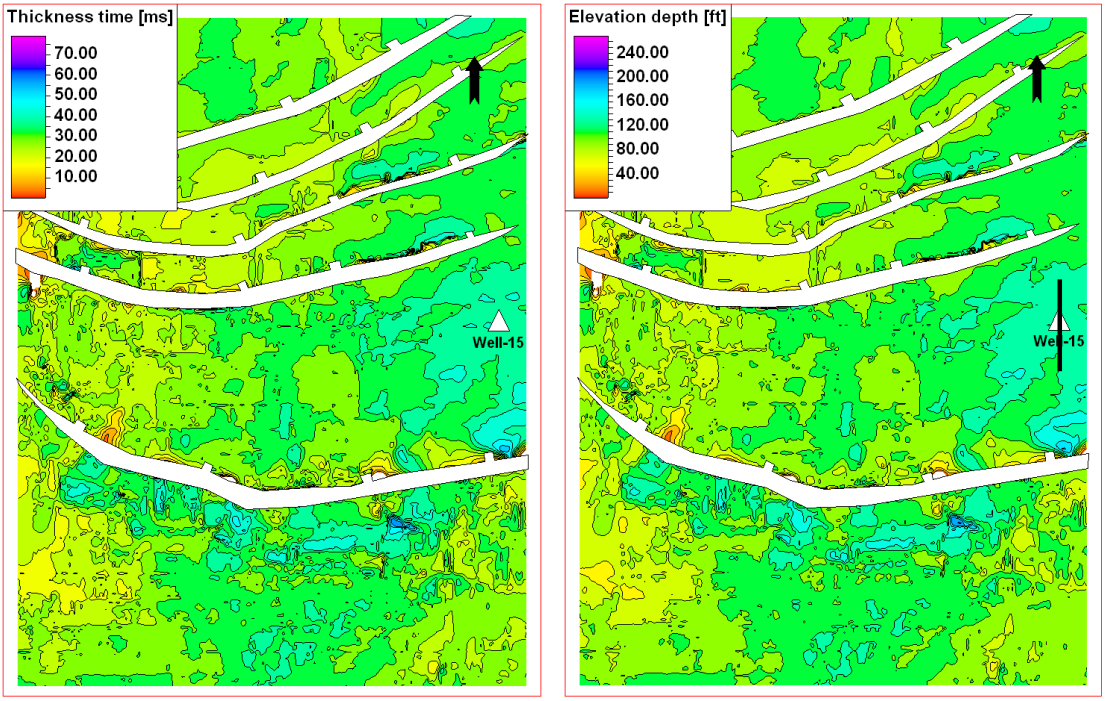

Figure 19. Time thickness map converted to depth.

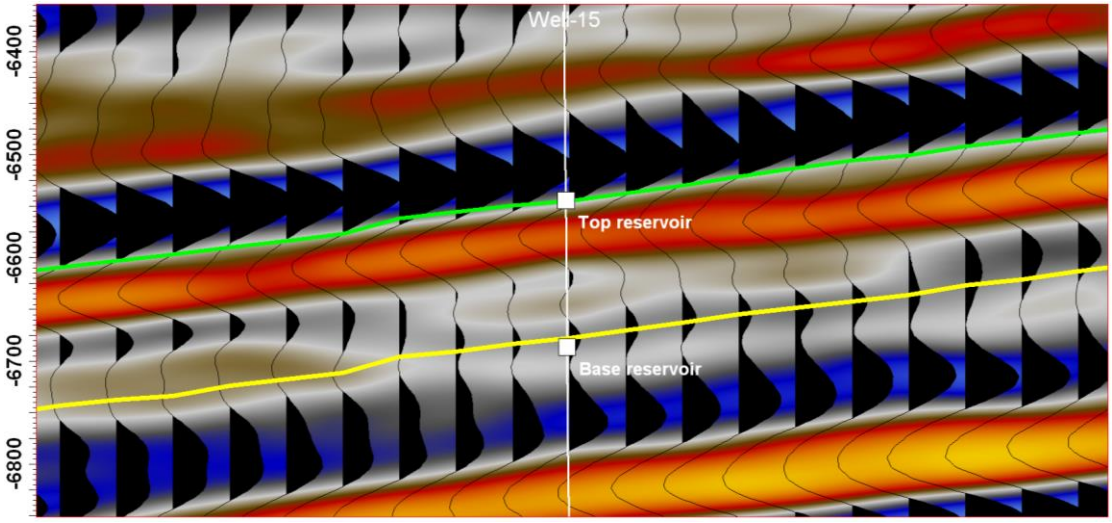

Figure 20. Base reservoir depth surface constructed from depth thickness map. Intersect given in figure 19.

3.4 STRUCTURAL MODELING

The goal of building the 3-D models for this study is to calculate reservoir volumes. Figure 21 illustrates the three steps involved in creating a structural model in the used modeling package (Petrel). The first step defines the fault planes of the

geological model as a set of linear key pillars that form the basis of creating the 3-D grid. The second step uses the pillars from the faults to construct a skeleton grid, which guides the geometry of the final 3-D grid. The final step is to insert horizons and, if necessary, zones defined by well tops only into the skeleton grid. This process defines the 3-D grid. Often modeling the seismic horizons require manual editing to ensure that the horizon-fault intersects are correct.

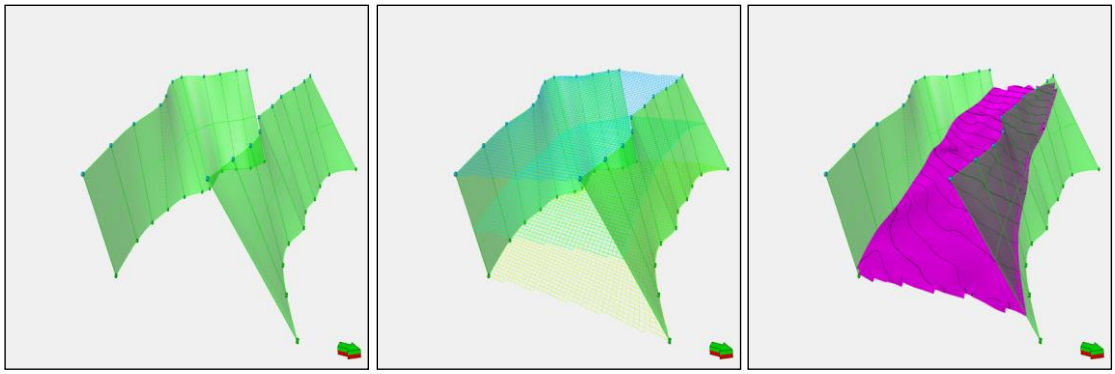

Figure 21. Structural modeling. Fault modeling (left), pillar gridding (middle) and horizon modeling (right).

3.5 EXPERIMENTAL DESIGN

Experimental design applies multiple linear regression analysis to several independent variables (X) to make an analytical relationship with a measurable output (V_{pred}). The used method assumes a linear relationship between X and V_{pred}, represented by a proxy equation:

$$V_{pred} = \beta_0 + \beta_1 X_1 + \beta_2 X_2 \ldots \beta_n X_n \quad (3.4)$$

where the β_n coefficients reflect the contribution to the output of each corresponding X_n factor, where n is the number of factors under consideration. The factors represent the model parameters. This study considers six parameters, i.e. two faults, time horizon, time thickness, depth horizon and depth thickness. V_{pred} is the

predicted reservoir volume based on the value of the parameters. In order to solve the coefficients (β_n) a set of linear equations (n+1) for different parameter sets and corresponding reservoir volumes is solved through multiple linear regression analysis. The parameters can have values within the range of [-1, 1] with minus one describing the low case, zero the base case and plus one the high case parameter. Table 2 shows the matrix of the screening design used and the parameter sets for which the reservoir volume needs to be calculated. This involves building 3D models using these parameter sets and calculating the requested volumes.

Table 2. Experimental design matrix.

Exp #	Fault1	Fault2	HorizonT	ThicknessT	HorizonD	ThicknessD	Resp_Volume
1	1	-1	1	-1	-1	-1	
2	-1	-1	-1	-1	-1	-1	
3	-1	-1	1	1	1	-1	
4	1	1	1	-1	1	1	
5	1	1	-1	1	-1	-1	
6	1	-1	-1	-1	1	1	
7	0	0	0	0	0	0	
8	-1	1	1	1	-1	1	
9	-1	1	1	-1	1	-1	
10	1	1	-1	1	1	-1	
11	1	-1	1	1	-1	1	
12	-1	1	-1	-1	-1	1	
13	0	0	0	0	0	0	
14	-1	-1	-1	1	1	1	

For example, consider a linear equation describing the reservoir volume as a function of one parameter (Horizon):

$$V_{pred} = \beta_0 + \beta_1 * Horizon \quad (3.5)$$

First, the coefficients β_0 and β_1 are calculated from two equations with the parameters and volumes given below:

Experiment	Horizon	Response Volume (V)
1	0	30
2	-1	10

The first equation is the centerpoint of the regression model, and delivers the value of the β_0 coefficient (30). Subsequently, the β_1 coefficient is derived using simple algebra,

$$\beta_1 = \frac{V - \beta_0}{Horizon} = 20$$

With,

$$V = 10$$

$$Horizon = -1$$

$$\beta_0 = 30$$

Now the reservoir volume distribution can be computed by solving the equation (5) several hundred times through stochastically varying the parameter values within the range [-1, 1] as shown below.

Prediction	Horizon	Predicted Volume (V_{pred})
1	-0.2	26
2	0.91	48.2
3	1	50

4	0.34	36.8

This study applies a Plackett-Burman design (Plackett *et al.,* 1946) for screening the reservoir parameters in order to understand their influence on the volume. Screening designs assume that all interactions are negligible this delivers a less accurate proxy equation (3.6). The number of experimental runs required is dependent on the parameters under consideration and the saturation level of the model. The benefit of Placket-Burman designs, as implemented in the used software (Essential Experimental Design, (Steppan *et al.,* 1998)), is that they only require twelve experimental runs plus two centerpoints for up to eleven factors. In other words, they utilize all degrees of freedom to estimate the main terms (Steppan *et al.,* 1998). These results are accurate enough for identifying the most influential parameters on the calculated volume.

$$V_{pred} = \beta_0+\beta_1X_1+\beta_2X_2+\beta_3X_3+\beta_4X_4+\beta_5X_5+\beta_6X_6 \quad (3.6)$$

The uncertainty analysis of the reservoir volume is based on those coefficients that contribute more than 5% to the total volume.

Based on the most influential parameters a two-level full factorial experimental design has been selected for setting up the proxy equation used for predicting the volume distribution resulting from the parameter uncertainties. A two-level full factorial design includes two- and three-way interactions in addition to the main terms. A two-level full factorial design requires 2^n experimental runs and two centerpoints, where the constant 2 represents the high and low setting coming from

each factor and n represents the number of factors used to model the predicted volume (Steppan *et al.,* 1998).

$$V_{pred} = \beta_0+\beta_1X_1+\beta_2X_2+\beta_3X_3+\beta_4X_4+\beta_5X_5+\beta_6X_6+\beta_7X_1X_2 + \cdots + \beta_aX_1X_2X_3 + \cdots \quad (3.7)$$

The number of terms in the full factorial proxy equation (3.7) is dependent on the results from the screening design. Equation 3.7 can contain statistically insignificant terms. Backward elimination measures the significance value for each term, where low values indicate high model significance (Steppan *et al.,* 1998). If a term exceeds a preconditioned significance value it is not included in the volume equation. The resulting equation, with fewer terms, is regarded as the best-fit model to predict the volume.

4. Observations

4.1 SYNTHETIC SEISMOGRAM OBSERVATION

Synthetic seismograms were constructed for three wells that have sonic and density logs covering the reservoir interval to identify the geologic events on the seismic data. Figure 22 shows that the seismic data has SEG polarity: the upper part of the figure shows the synthetic trace in inverse polarity, the lower part shows the normal polarity. The correlation trace gives maximum positive correlation for the synthetic trace in SEG polarity. A zero crossing between a strong peak reflection and a trough features the top of the reservoir on the synthetic traces of all three wells (Figure 23). The base of the reservoir is not as clearly defined and alternates between a faint peak reflection and an s-crossing, i.e. where the amplitude is zero between a trough at the top and peak reflector at the bottom.

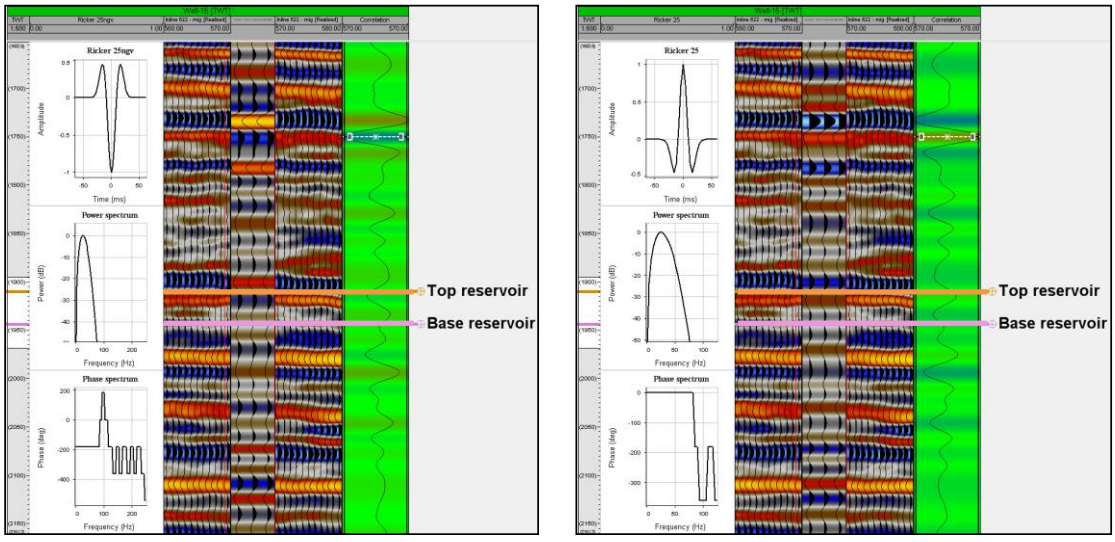

Figure 22. Synthetic seismogram from Well-15. First track shows a Ricker wavelet, which delivers the synthetic trace displayed in the middle of the seismic section. The last track (to the right) shows the correlation between the synthetic trace and the seismic trace closest to the well position.

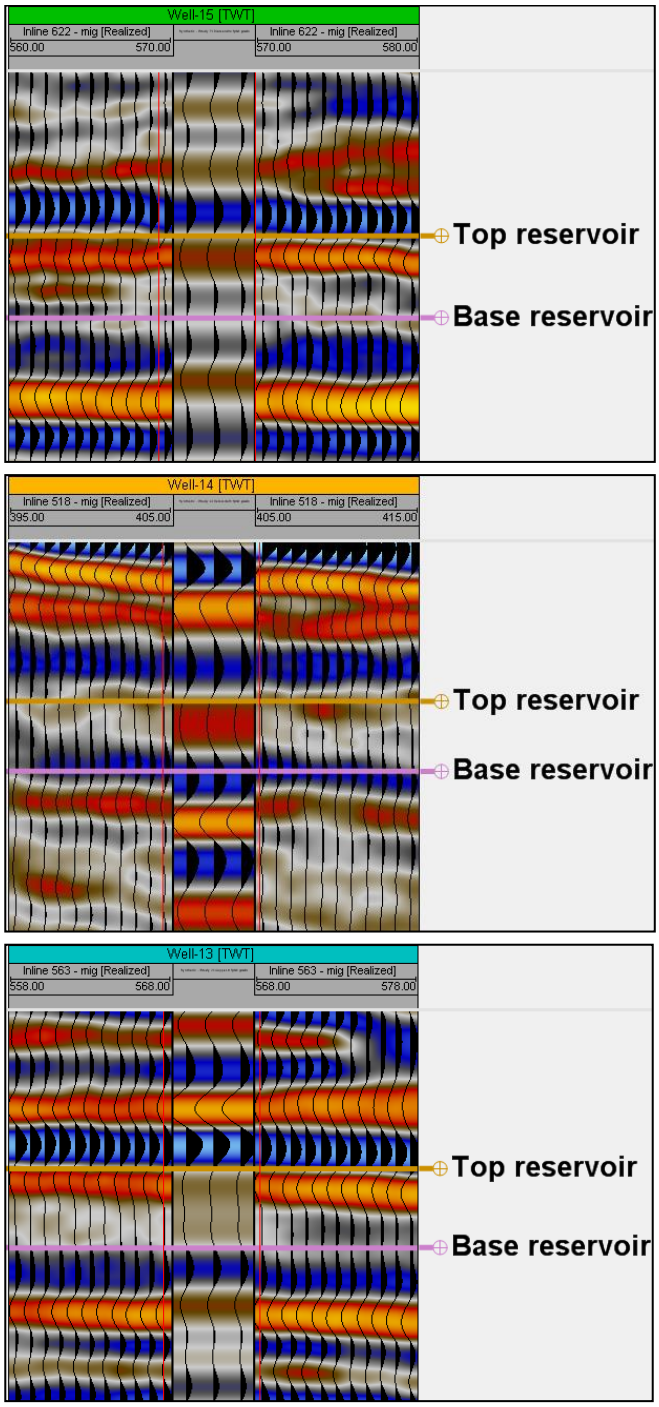

Figure 23. Synthetic seismogram from well-15 (left), well-14 (middle) and well-13 (right).

4.2 SEISMIC INTERPRETATION AND UNCERTAINTY ESTIMATION

4.21. Horizons

To illustrate the uncertainty in seismic interpretation requires the analysis of seismic sections with focus on comparing the original seismic volume with attribute cubes in areas of uncertainty, such as low signal-to-noise. Three random seismic lines crossing key wells were created for this purpose (Figure 24).

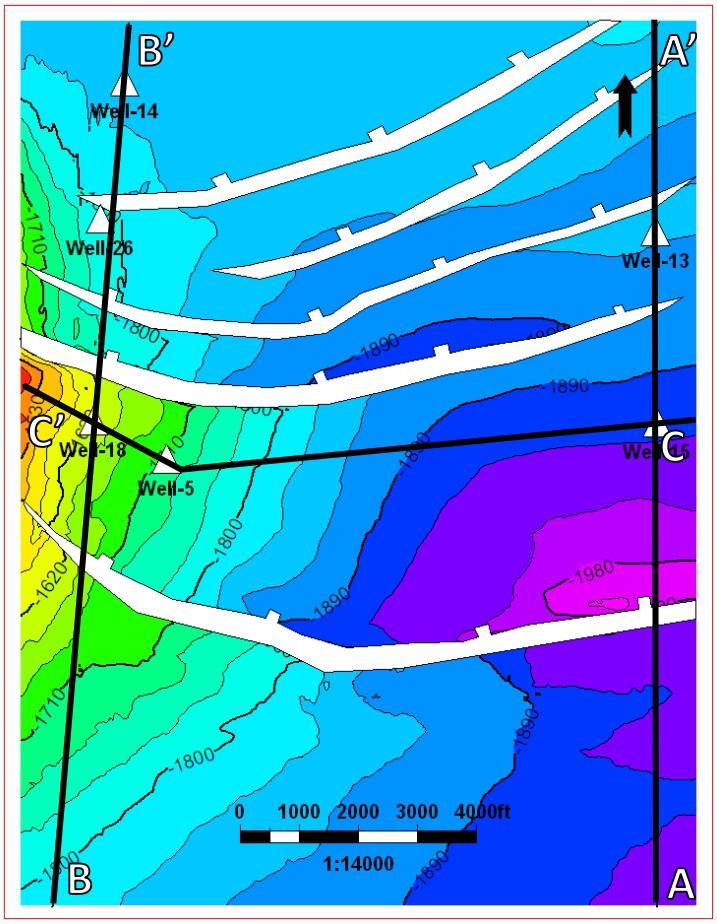

Figure 24. Time structure map of top reservoir, shows selected wells and seismic intersections.

These areas of uncertainty can be identified based on the following classification:

Class 1: Weak semi-continuous amplitude

Class 2: Low signal-to-noise ratio resulting in discontinuities

The navigation of the seismic sections discussed in the following is given in Figure 24. The frames shown in black on sections A – C (Figure 25, 28 and 32) correspond to the enlarged sections to highlight the areas of uncertainty. The seismic sections show that the top reservoir seismic event (shown in green) is tracked on a zero crossing between peak and trough reflectors with strong amplitudes. The base reservoir seismic event (shown in yellow) is tracked on a zero crossing between trough and peak reflectors with weak semi-continuous amplitudes.

In frame 1 and 2 on section A (Figure 25), strong amplitudes characterize the top reservoir throughout the section; whereas the base reservoir features class 1 and 2 uncertainties (Figure 26a and 27a). The cosine of instantaneous phase provides a better continuity of the base reservoir seismic event for the interpretation, which allows tracking the horizon in this area with more confidence (Figure 26b and 27b).

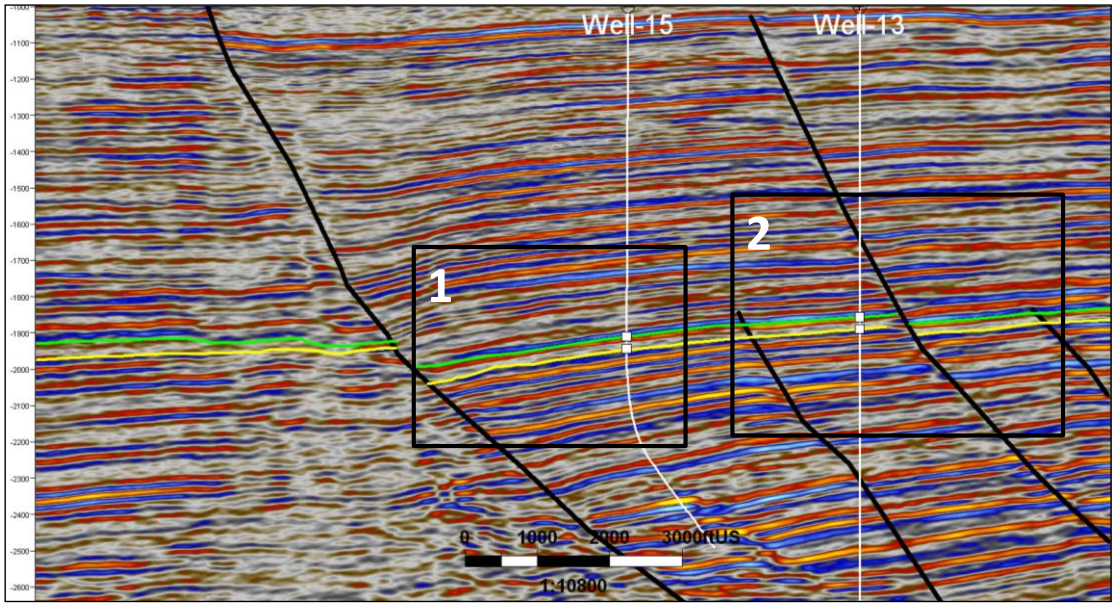

Figure 25. Section A, intersect shown on figure 24.

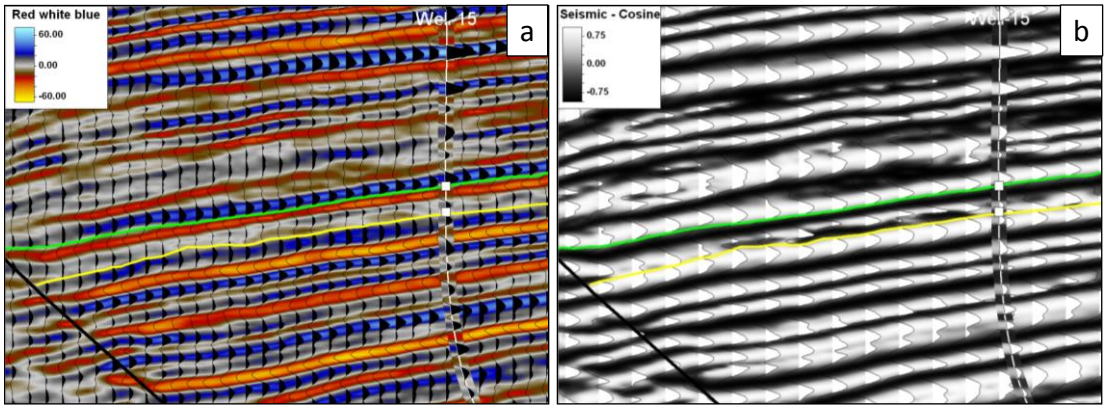

Figure 26. Section A, frame 1.

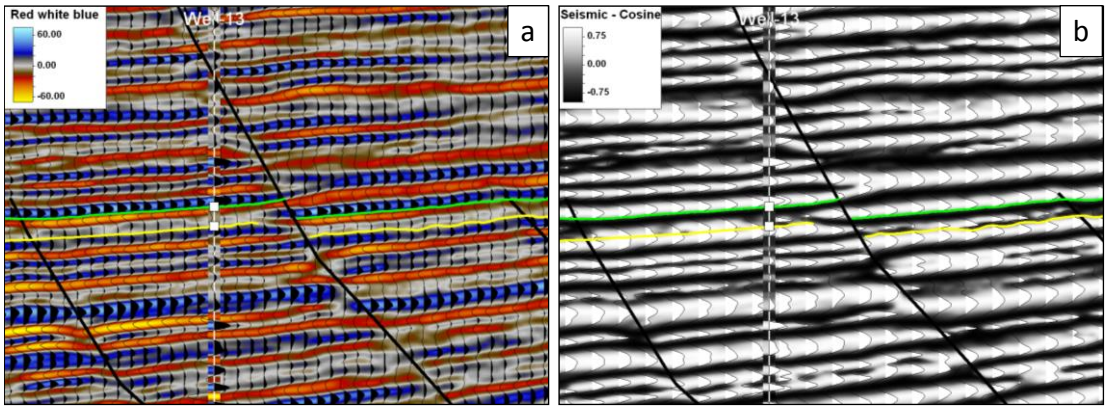

Figure 27. Section A, frame 2.

In frame 1 on section B (Figure 28), the two seismic events display class 1 uncertainty near a minor fault (Figure 29a). The structural smoothing attribute enhances the continuity of the downthrown events significantly (Figure 29b). In frame 2, the top reservoir horizon features class 1 uncertainty, and the base class 1 and 2 uncertainties (Figure 30a). Again, structural smoothing enhances the continuity of the top reservoir horizon, although on cost of the resolution, which is decreased near the base horizon (Figure 30b). In frame 3, the top reservoir features class 1 uncertainty, and the base class 1 and 2 uncertainties (Figure 31a). Structural smoothing enhances continuity and increases the signal-to-noise ratio (Figure 31b).

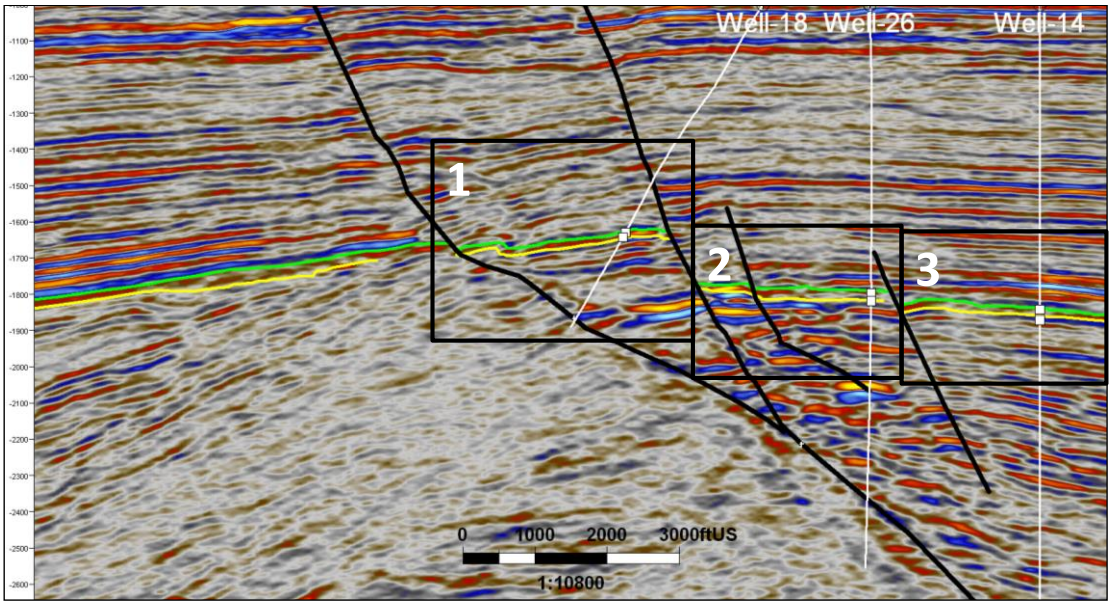

Figure 28. Section B, intersect shown on figure 24.

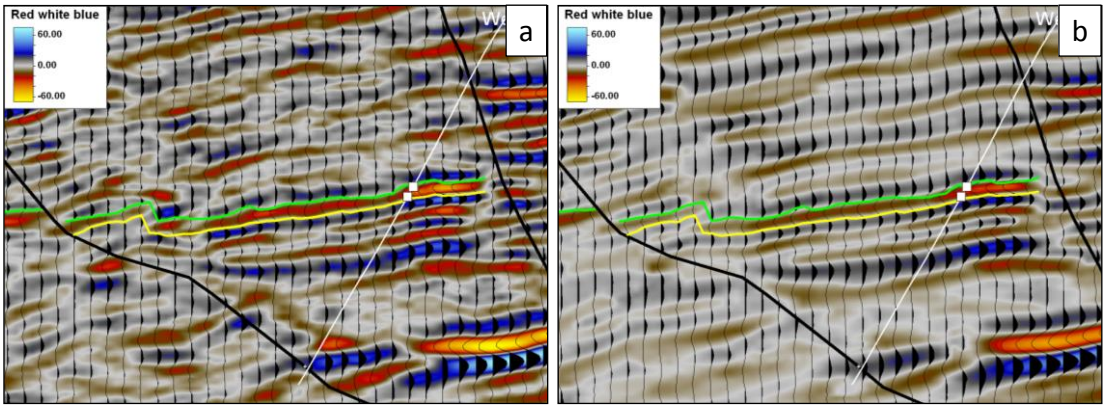

Figure 29. Section B, frame 1.

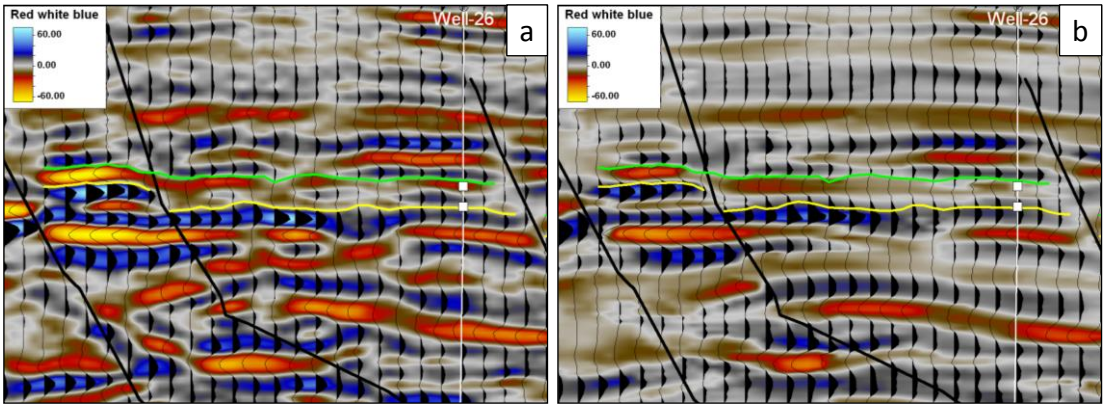

Figure 30. Section B, frame 2.

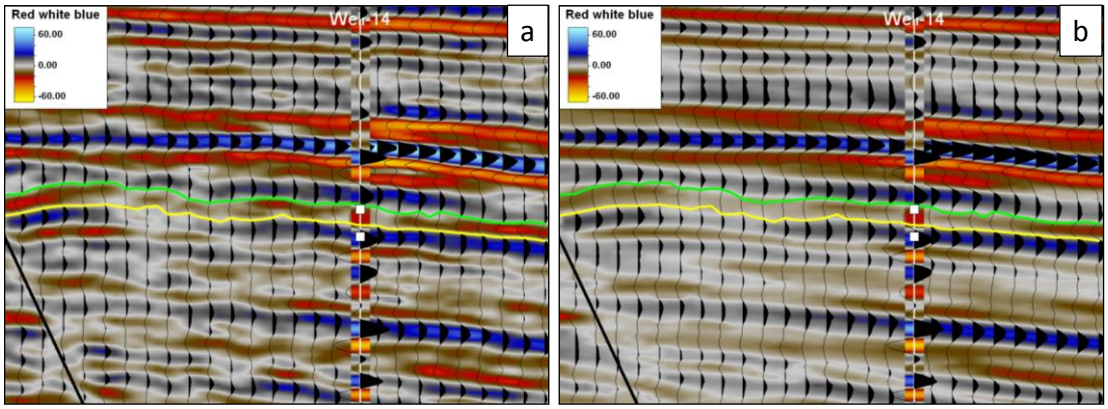

Figure 31. Section B, frame 3.

In frame 1 on section C (Figure 32), the top and base horizons feature class 1 uncertainty (Figure 33a). Structural smoothing enhances seismic continuity for the top horizon only (Figure 33b). In frame 2, the top reservoir horizon shows characteristics of strong amplitudes, whereas the base reservoir horizon features class 1 uncertainty (Figure 34a). Cosine of instantaneous phase provides better continuity of the base reservoir seismic event (Figure 34b).

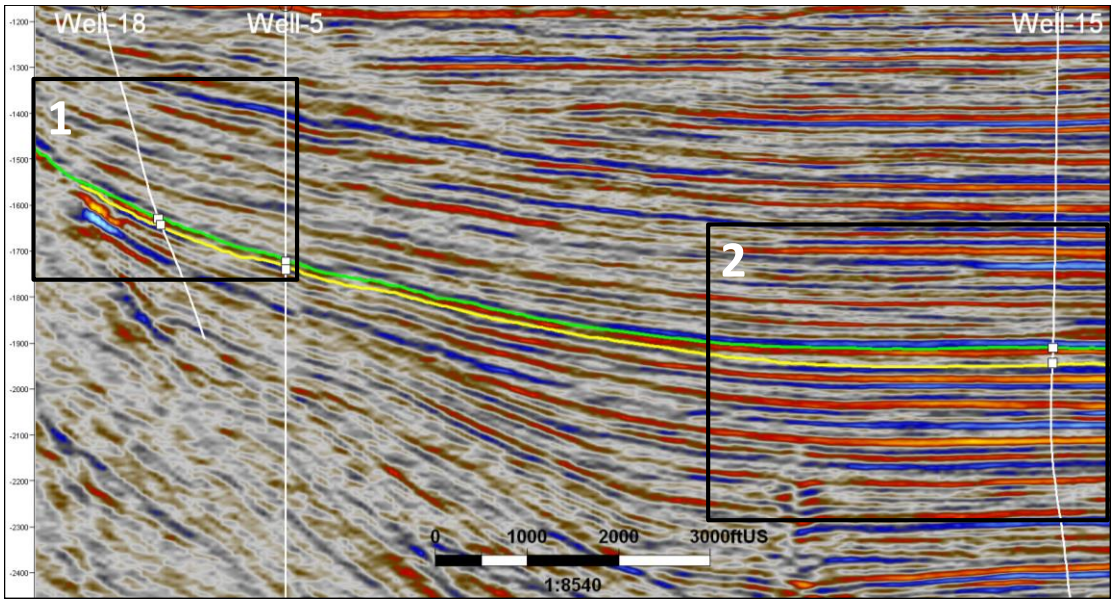

Figure 32. Section C, intersect shown on figure 24.

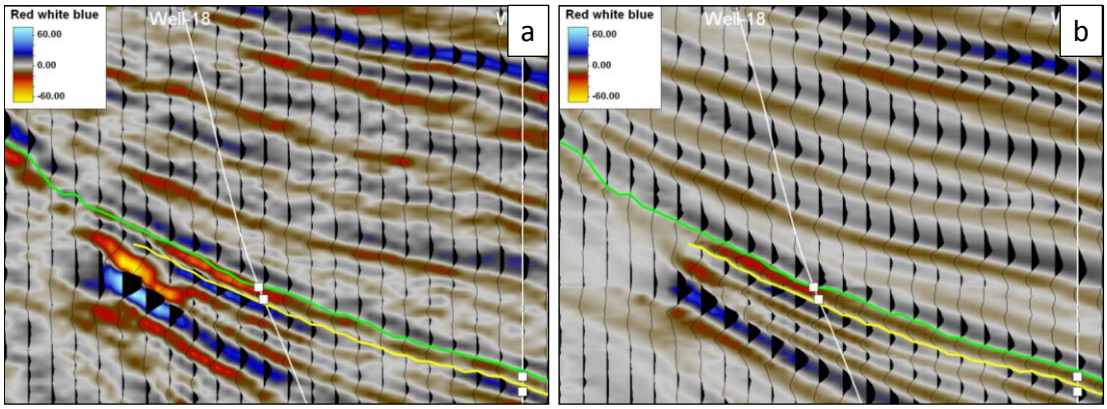

Figure 33. Section C, frame 1.

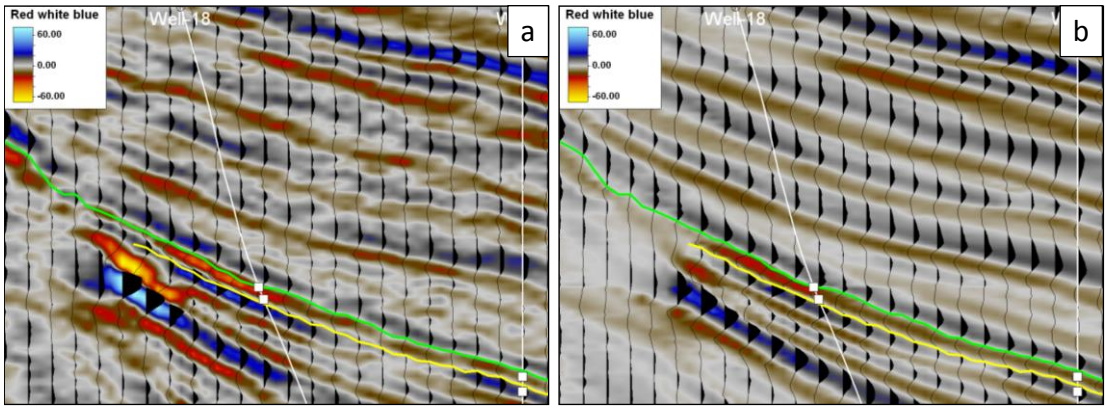

Figure 34. Section C, frame 2.

A difference map of the original seismic volume and a smoothed volume shows that uncertainties due to statics have a Gaussian distribution with a standard deviation of ± 1.32 ms (Figure35).

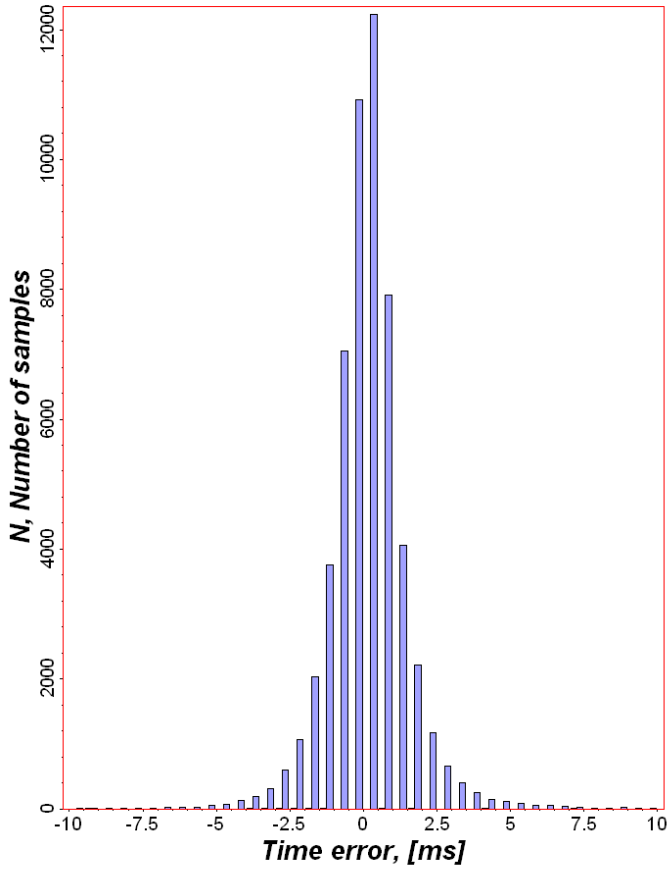

Figure 35. Time error distribution due to statics.

Tops on three wells show significant offset with respect to the seismic event (Figure 36). Well-11 and Well-8 are both in the vicinity of the tied Wells 13 and 14 respectively (Figure 36a and b). The tops of Well-19 are located on a different phase positioned in an isolated fault segment (Figure 36c). Following the seismic event linked to these well tops will result in a conflict with the interpretation supported by the other wells. Therefore, wells 8, 13 and 19 are not included in the uncertainty study.

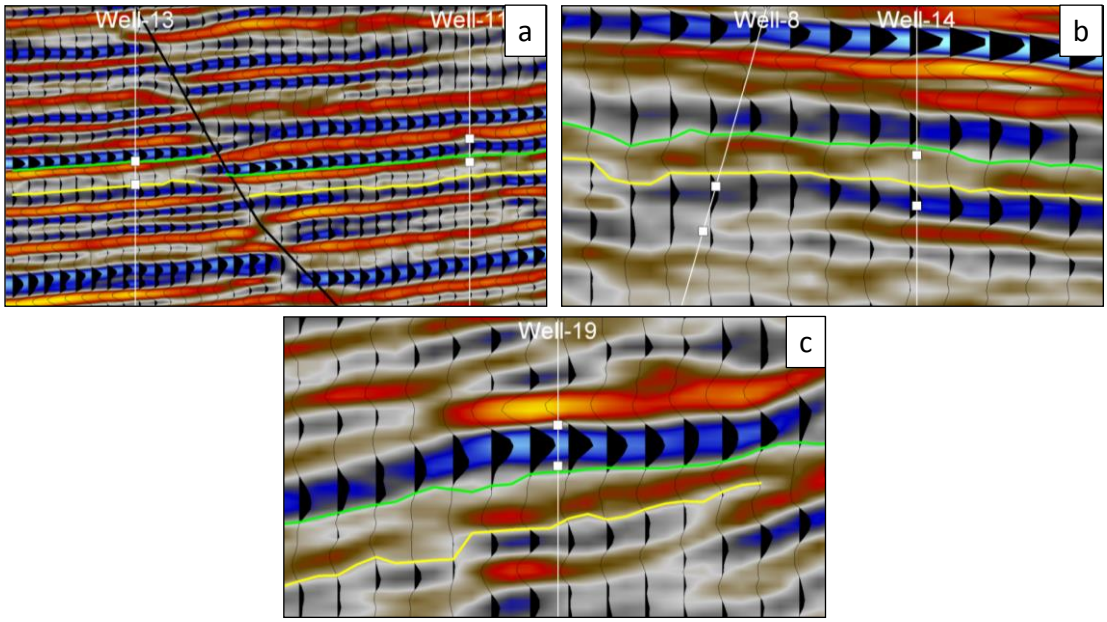

Figure 36. Seismic intersections showing offset wells.

The time error between the interpreted top reservoir horizon and each well top gives a distribution of time errors (Figure 37). Table 3 summarizes the time error statistics, of the top reservoir horizon and the reservoir thickness, used for constructing the high and low cases. The mean error of -1.83 ms for the top reservoir indicates that the geological event is about 2 ms below the tracked zero crossing. Applying the shift of -1.83 ms to the top reservoir results in a normal error distribution with zero mean. The base reservoir is constructed through stacking the reservoir time thickness below the top reservoir as discussed in the Methodology. The time error for the reservoir base is resulting from the reservoir thickness uncertainty (Figure 38).

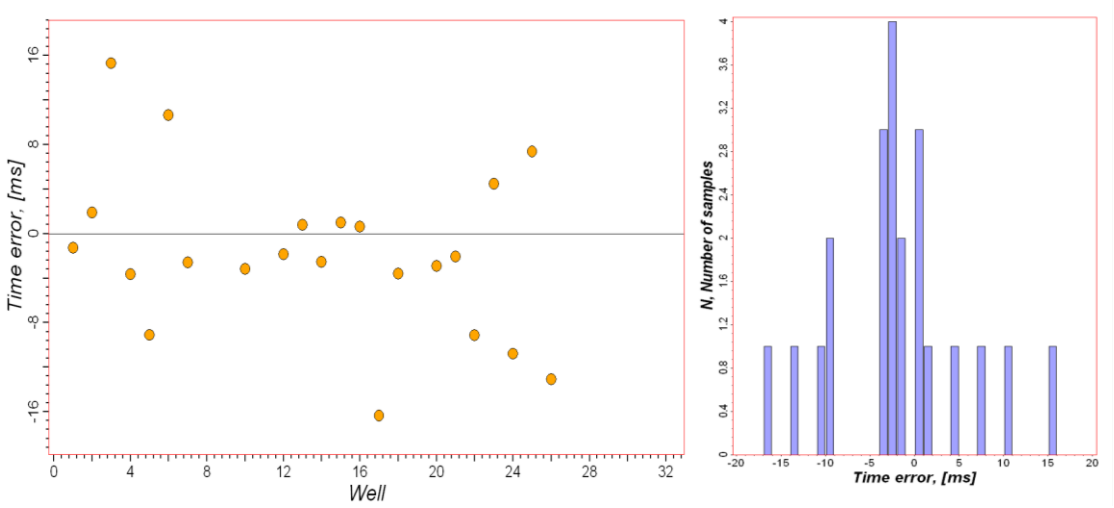

Figure 37. Time error distribution of the top reservoir.

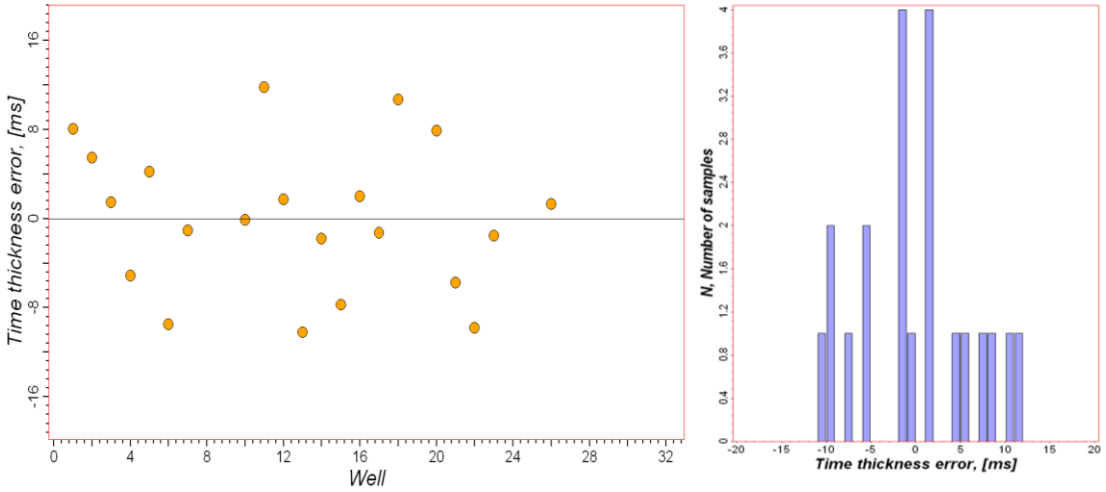

Figure 38. Time error distribution of the reservoir thickness.

Table 3. Time error statistics.

	Top reservoir (ms)	**Reservoir thickness (ms)**
Mean	-1.83	0
std.dev.	7.38	6.55
Variance	54.46	42.94

The sample variograms shown in Figure 39 and 40 define the spatial correlation of the time errors. The variogram model fitted to the variance points of the time errors shows that the influence radius of the wells (variogram range) has a range

of 600 feet for the top reservoir and 1000 feet for the reservoir thickness (Figure 39 and 40). These measurements are used for adjusting the top and base reservoir cases to the well tops.

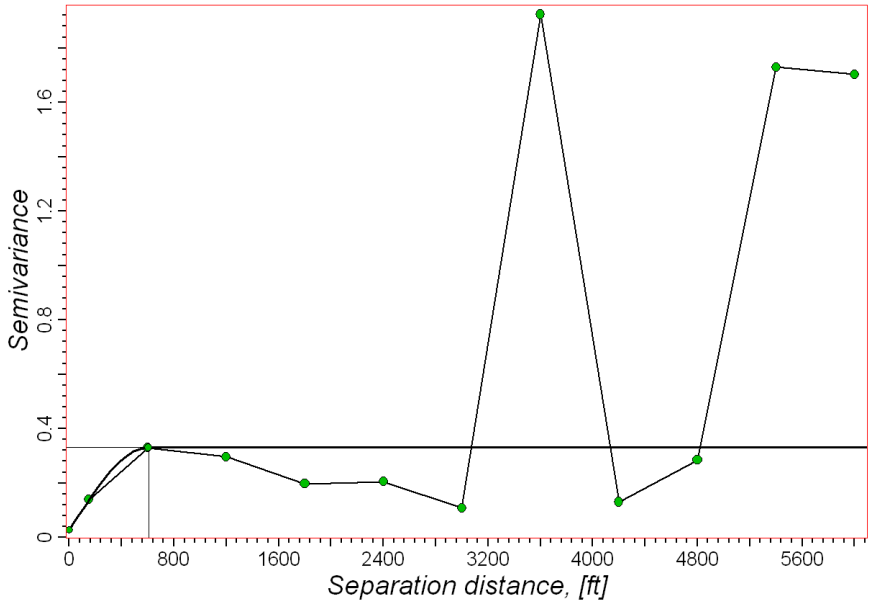

Figure 39. Variogram analysis of time errors for top reservoir, shown in figure 37.

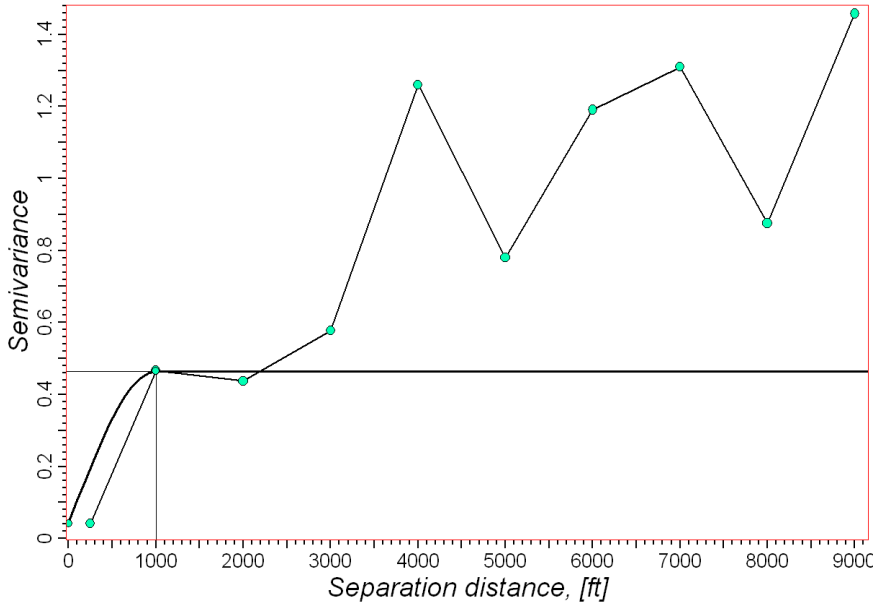

Figure 40. Variogram analysis of the reservoir thickness in the time domain, shown in figure 38.

4.2.2 Faults

The ant track volume captures the two faults outlining the reservoir fairly well within most of the seismic volume (e.g. section A, Figure 41). The time lines of the ant tracking time slices in Figure 42 are also included in Figure 41. In Figure 41 and 42 the faults representing the base case are shown in green, the faults capturing the fault zone outline are shown in red and blue. Both faults are represented by the offset of strong amplitudes in the reservoir. However, the southern fault shows more bifurcation on the ant tracking time slices resulting in a wider uncertainty envelope. In addition, the westernmost area between -1700 and -1900 ms shows the southern fault changing its strike significantly. Here the characteristics for fault detection are weak and not captured by the ant track volume (Figure 41 and 42). The continuation of the fault can be seen below -1900 ms, where it is truncated by the northern fault.

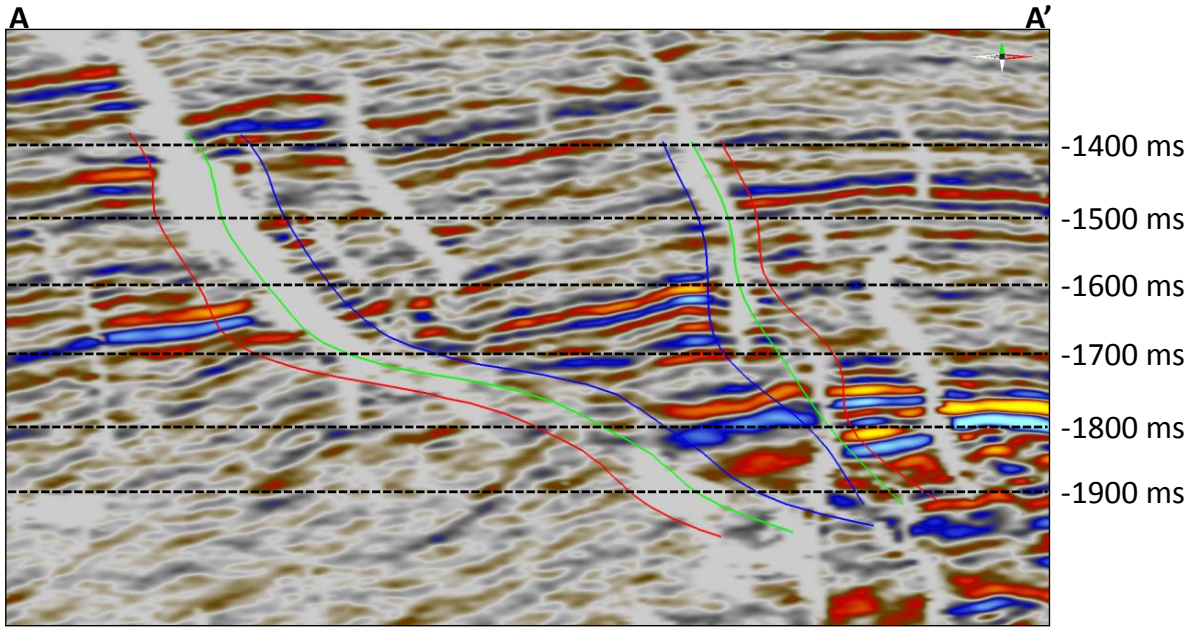

Figure 41. Section A, intersect shown on figure 42 (top left).

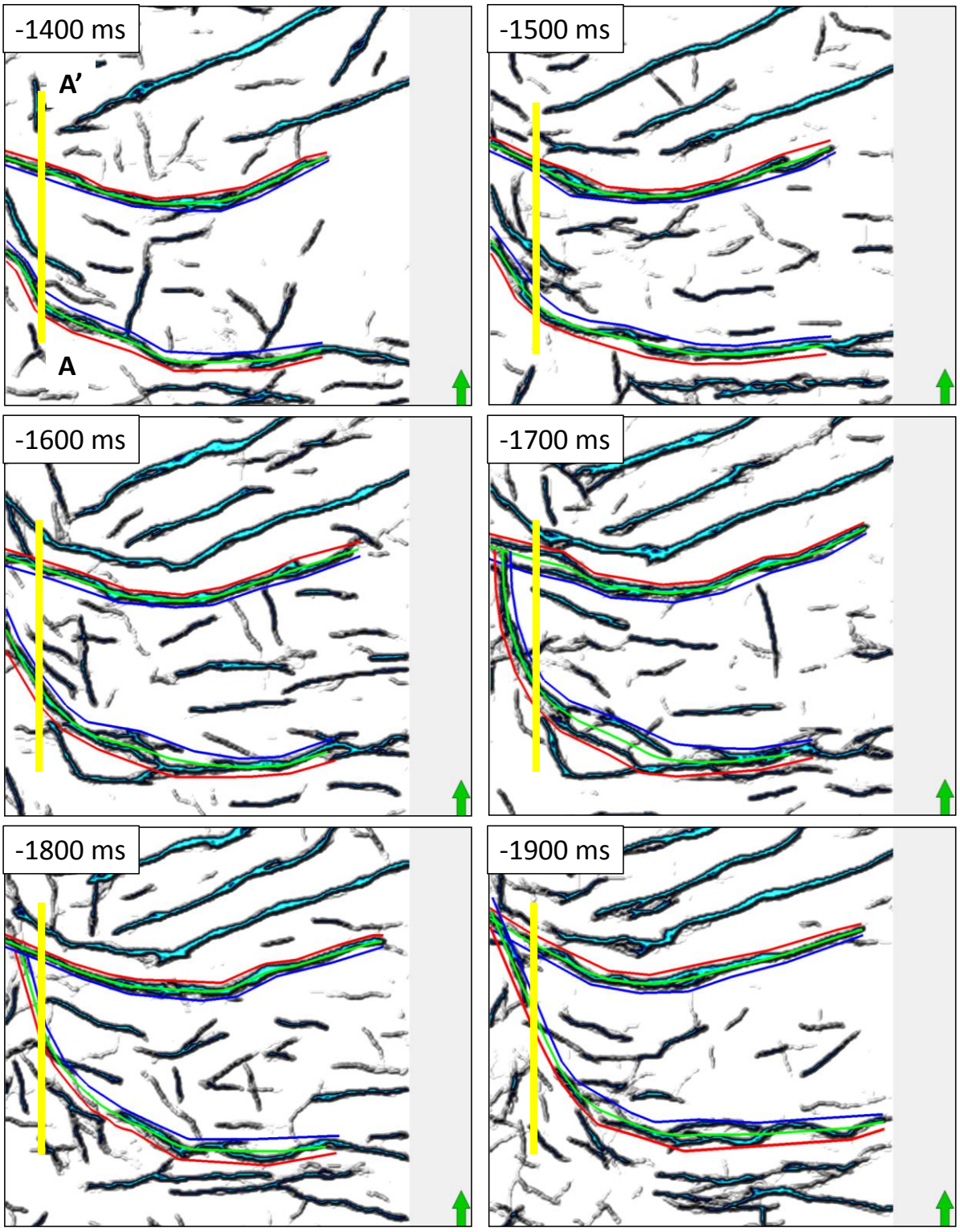

Figure 42. Time slices from ant track volume.

The apparent average thicknesses of the northern and southern faults defined by the fault envelopes are 466 ft and 765 ft, respectively. These thicknesses were calculated from the difference between polygon nodes in a consecutive order (see Figure 12). In order to quality check the apparent thickness of the fault envelope fault slicing has been applied. Figure 43 shows the fault slicing results for the northern fault using a step-out distance of 150 and 233 ft. Most of the amplitudes fade out at a step out distance of ± 233 ft from the base case fault. The bifurcation and low quality imaging of the southern fault yields imperceptible results.

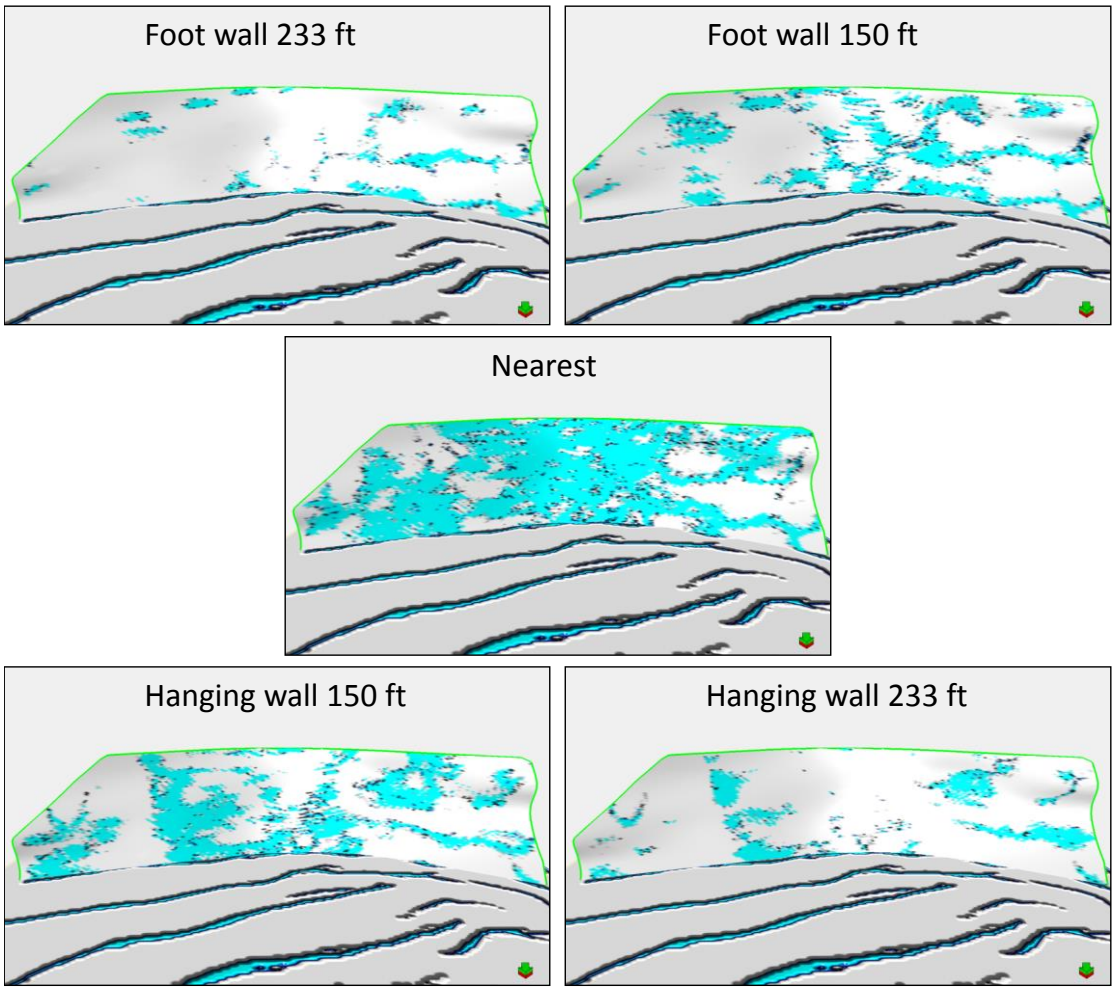

Figure 43. Fault slicing of the northern fault.

4.3 DEPTH CONVERSION

4.3.1 Linear velocity law

Figure 44 shows the relationship between the interval velocities coming from the check shots and the derived linear velocity law for two wells. The check shot velocities show a velocity boundary marked as the overburden horizon. Below the overburden boundary, the slope of the linear velocity law changes. For the reservoir interval, a constant interval velocity has been selected, which is shown by the straight vertical line in Figure 44.

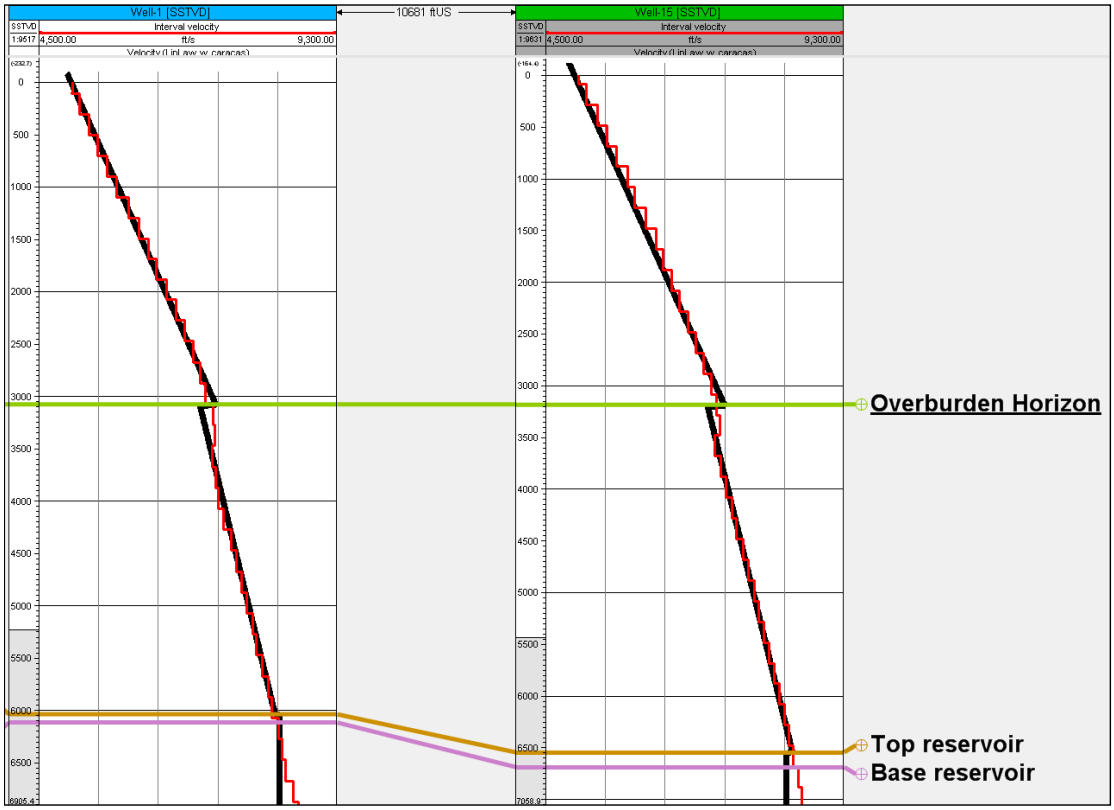

Figure 44. Linear velocity law (black) and checkshot interval velocities (red) from Well-1 and Well-15.

As discussed in the methodology chapter, the K-value of each of the two linear velocity laws of the overburden is constant. The V_0 values are extracted at the layer

top and interpolated away from the wells. The selected gridding algorithm influences the resulting depth surface. Figure 45 shows the depth conversion of the top reservoir surface based on two different gridding algorithms applied to the V_0 data. The moving average gridding algorithm ensures that the V_0 approaches a constant average value at some distance away from the wells. Convergent interpolation uses the slopes defined by the data points and therefore can interpolate and extrapolate to unrealistic values. A comparison of the depth surfaces resulting from the two V_0 interpolations shows considerable differences. This is highlighted in Figure 46, which shows the difference map between the two depth surfaces and the histogram of the depth differences.

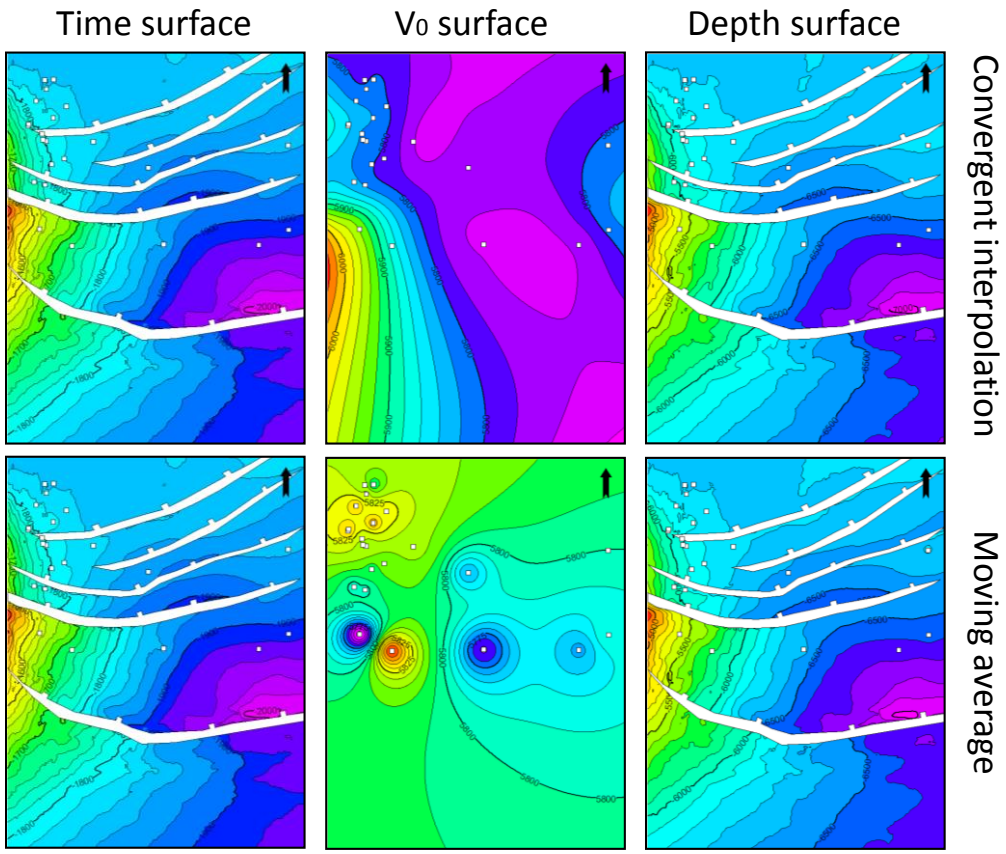

Figure 45. Problems in depth conversion. Time structure map of top reservoir (left), Initial velocity surface (middle) and depth structure map of top reservoir (right).

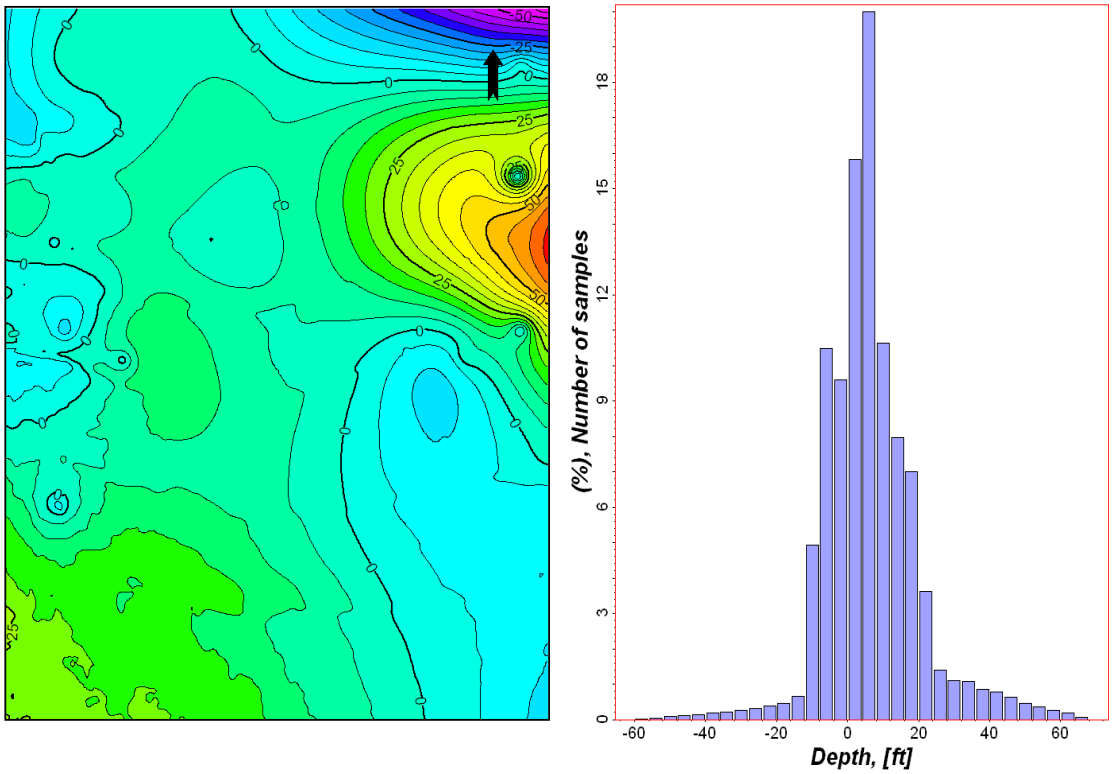

Figure 46. Difference map of the two depth surfaces of the top reservoir based on V0 interpolation using Convergent Interpolation and Moving Average, respectively.

4.3.2 Blind well test for estimating uncertainty in depth

Fifteen out of twenty-five wells were selected for the blind well test to avoid a cluster effect (Figure 47). The left out well is not taken into account for the extraction of the velocity law for the top two layers up to the reservoir top. The blind well test predicts that the depth surface uncertainty can lie within a probability interval described by the depth error distribution (Figure 48). Variogram analysis of the depth errors shows that their influence radius is about 900 feet (Figure 49).

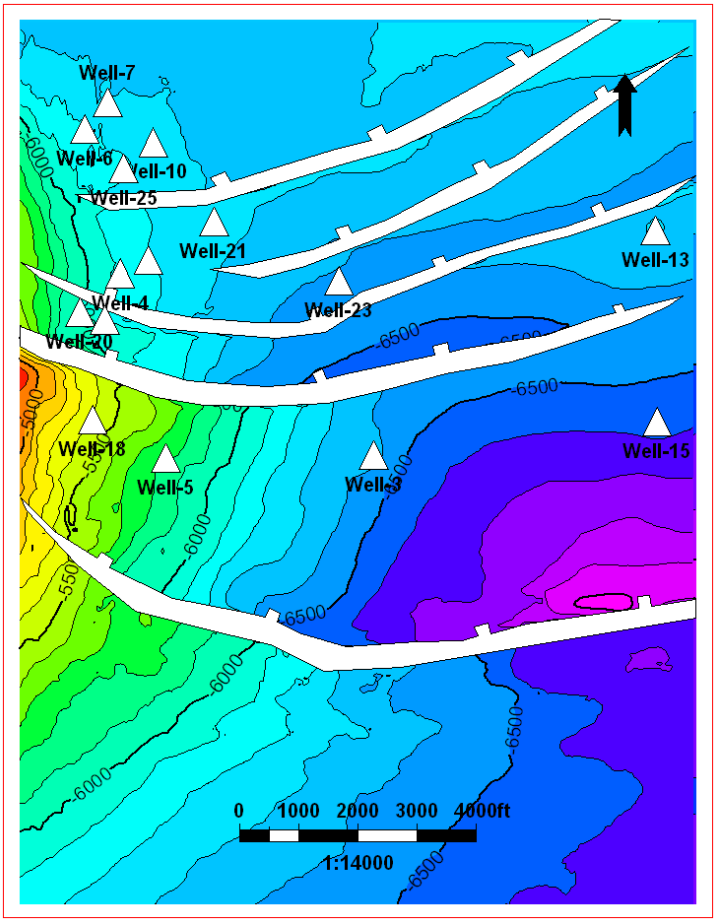

Figure 47. Depth structure map of top reservoir, wells used for the blind well test are shown.

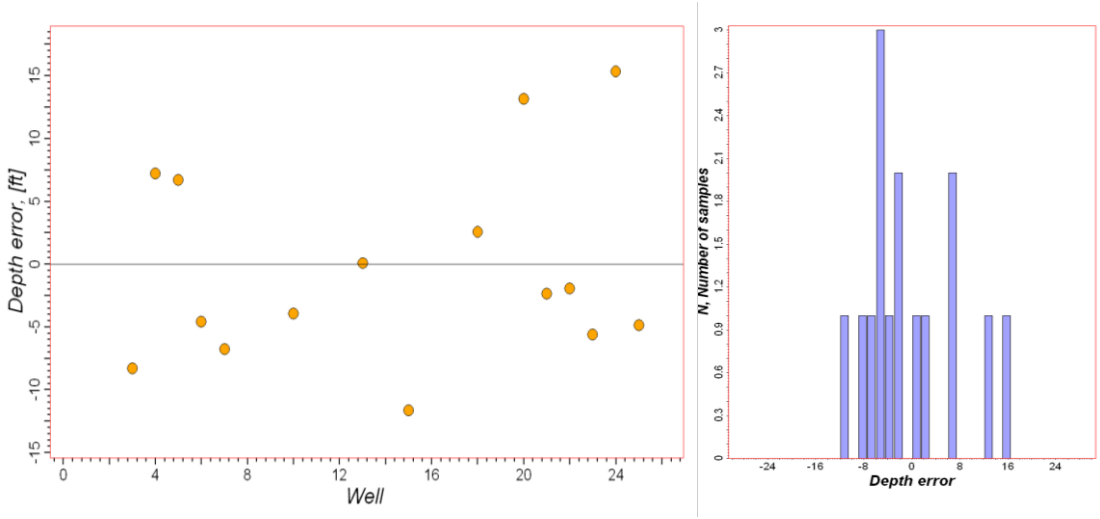

Figure 48. Depth error distribution of the top reservoir based on the blind well test.

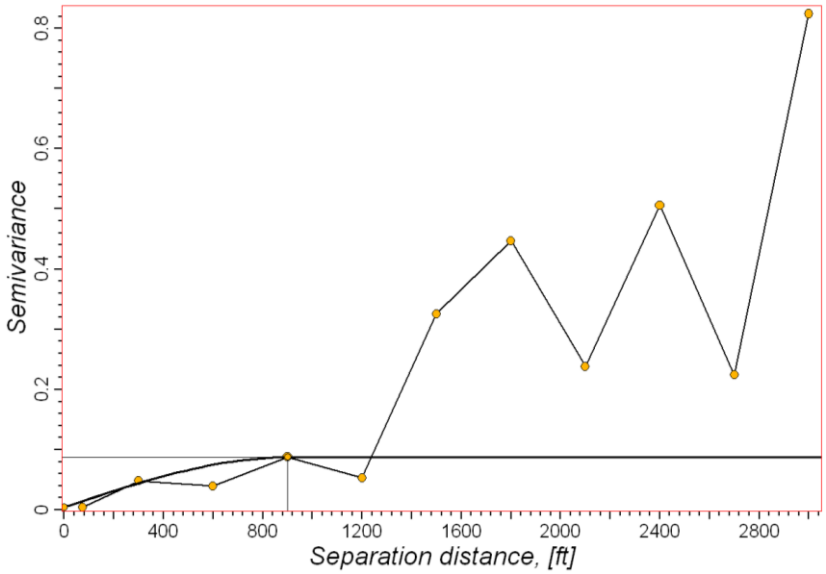

Figure 49. Variogram analysis of depth errors shown in figure 48.

The reservoir base shows a depth error at each well as a result of using the averaged interval velocity. The depth error distribution for the reservoir base is resulting from the reservoir thickness uncertainty (Figure 50). It is important to note that this approach requires that the top reservoir depth surface is adjusted to the well tops. Variogram analysis of the depth thickness errors shows that their influence radius is about 1000 feet (Figure 51). Table 4 summarizes the depth error statistics, of the top reservoir depth surface and the reservoir thickness used for constructing the high and low cases.

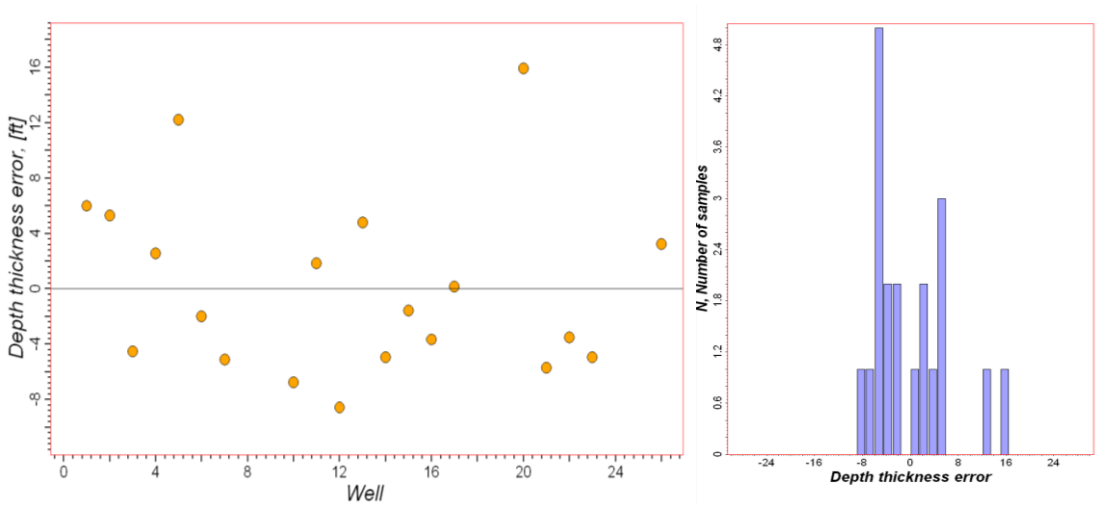

Figure 50. Thickness depth error distribution.

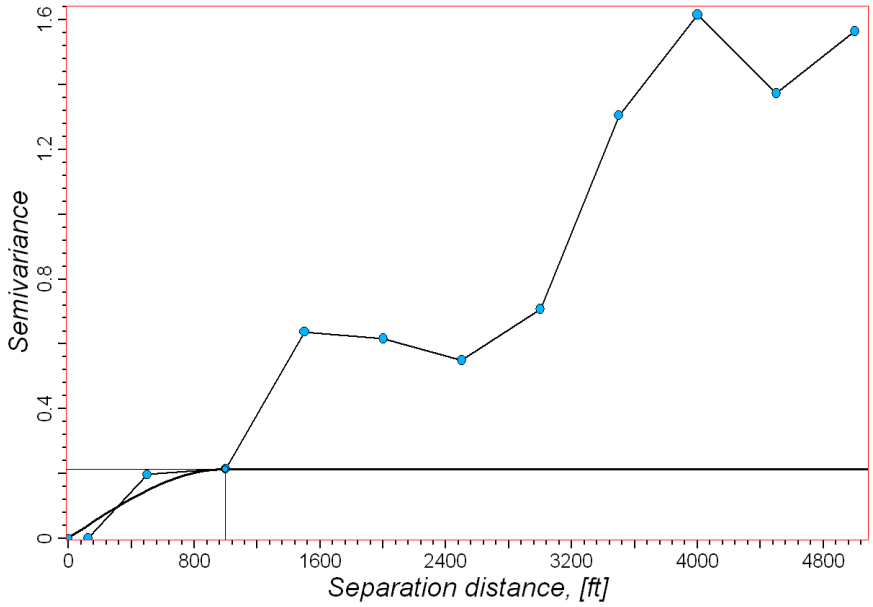

Figure 51. Variogram analysis of depth thickness errors in figure 50.

Table 4. Depth error statistics. The two columns for the top reservoir show the results from the blind well test using the moving average and convergent interpolation gridding algorithm, respectively.

	Top reservoir (ft)		Reservoir thickness (ft)
Mean	0	-8.67	0
Std.dev	7.84	46.76	12.05
Variance	61.52	2186.63	145.23

4.4 UNCERTAINTY IN GROSS-VOLUME DERIVED FROM MODELLED STRUCTURAL UNCERTAINTY

The Placket-Burman experimental design requires only fourteen structural models to solve the coefficients of the proxy equation, as discussed in the methodology chapter. The combinations of experimental runs and their results are summarized in Table 5.

Table 5. Combinations and volume results of structural models for the Placket-Burman experimental design.

Exp #	Fault 1	Fault 2	HorizonT	ThicknessT	HorizonD	ThicknessD	Volume
1	1	-1	1	-1	-1	-1	56.2
2	-1	-1	-1	-1	-1	-1	32.5
3	-1	-1	1	1	1	-1	122.6
4	1	1	1	-1	1	1	112.8
5	1	1	-1	1	-1	-1	109.9
6	1	-1	-1	-1	1	1	72.8
7	0	0	0	0	0	0	97
8	-1	1	1	1	-1	1	142
9	-1	1	1	-1	1	-1	72.7
10	1	1	-1	1	1	-1	128.6
11	1	-1	1	1	-1	1	142
12	-1	1	-1	-1	-1	1	56
13	0	0	0	0	0	0	97.2
14	-1	-1	-1	1	1	1	111.7

The Placket-Burman design is not accurate enough to derive a representative proxy equation for the volume. Figure 52a shows that the observed volume and the volume predicted by the proxy equation resulting from the Placket-Burman experimental design have a linear relationship. However, the residual plot of the difference between volumes of the proxy equation and the model volumes shows values up to $8*10^7$ ft^3 (Figure 52b). The Placket-Burman experimental design gives a

good estimation of the influence of the individual parameters on the predicted volume.

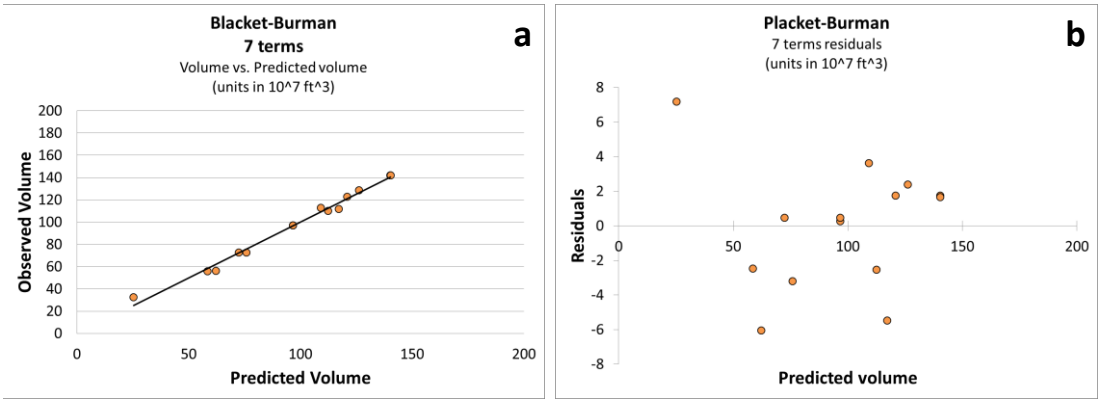

Figure 52. Placket-Burman experimental design. a) Observed volume vs. Predicted volume. b) Residual plot.

The Tornado diagram in Figure 53 graphs the coefficients high and low setting for each parameter as an illustration of their volume contribution. The time thickness accounts for an uncertainty about 30,5% of the base case volume. The time horizon and the depth thickness account for an uncertainty about 12% and 10%, respectively. The two faults and the depth horizon each account for an uncertainty about 7% of the base case volume. This shows that all parameters are statistically significant for describing the structural volume uncertainty.

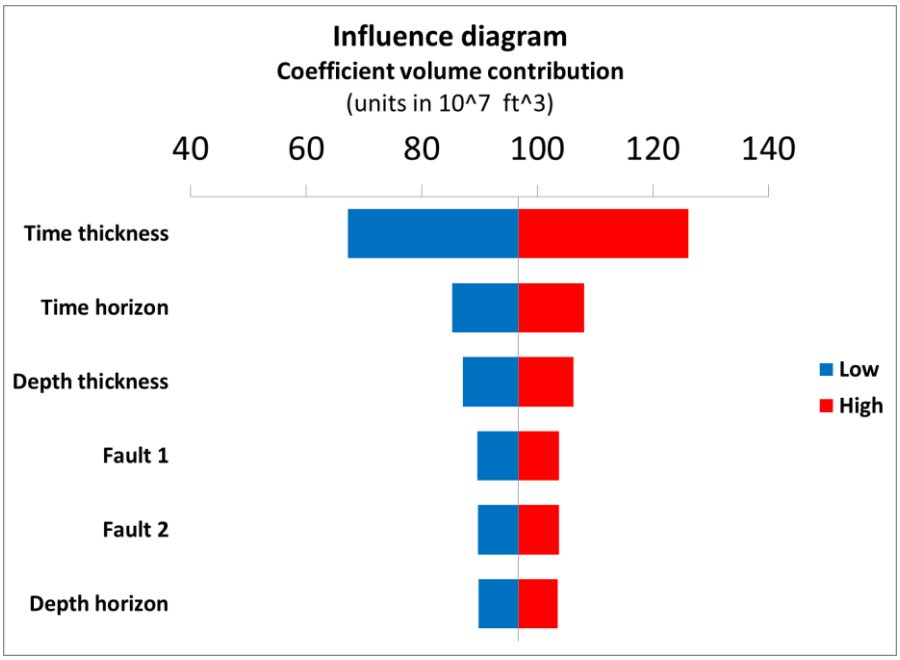

Figure 53. Influence of parameters on the base case volume.

The full factorial experimental design uses all six parameters. As a result, sixty-six structural models were created to derive the coefficients of the volume equation. The combinations of experimental runs and their results are summarized in table 6.

Table 6. Combinations and volume results of structural models for the full factorial experimental design

Exp #	Fault 1	Fault 2	HorizonT	ThicknessT	HorizonD	ThicknessD	Volume
1	-1	-1	-1	1	-1	-1	85.2
2	1	1	-1	-1	1	-1	57.9
3	1	-1	-1	-1	-1	-1	35.5
4	-1	1	-1	-1	-1	1	54.9
5	1	-1	-1	-1	1	1	67.9
6	-1	1	-1	1	-1	1	113.4
7	1	-1	-1	-1	-1	1	56
8	1	1	1	-1	-1	-1	60.5
9	-1	-1	1	1	1	1	138.2
10	-1	1	1	1	-1	1	142
11	1	1	1	1	-1	-1	144.3
12	1	-1	1	1	-1	1	142
13	0	0	0	0	0	0	97.2
14	-1	-1	-1	-1	1	-1	45.9
15	-1	-1	1	-1	1	-1	63.3

16	-1	-1	1	1	-1	-1	107.1
17	-1	-1	-1	1	-1	-1	85
18	1	1	-1	-1	-1	1	61.6
19	1	-1	-1	1	-1	-1	96.6
20	1	-1	-1	1	1	-1	109.9
21	1	-1	-1	1	-1	-1	96.6
22	1	1	-1	1	-1	-1	109.9
23	-1	1	1	1	1	-1	141.4
24	-1	-1	-1	1	1	1	111.7
25	1	1	1	-1	1	-1	79.8
26	1	1	1	1	-1	1	161.5
27	-1	-1	-1	-1	1	1	62.2
28	1	1	-1	1	1	-1	128.6
29	-1	1	-1	-1	1	-1	52.8
30	-1	1	1	-1	-1	-1	56.2
31	-1	1	-1	1	-1	1	113.3
32	-1	1	-1	1	1	1	129.2
33	1	-1	1	1	-1	-1	122.7
34	1	1	-1	-1	-1	-1	42.1
35	-1	1	-1	1	1	-1	113.3
36	0	0	0	0	0	0	97
37	-1	-1	1	1	-1	1	123
38	1	-1	1	1	1	-1	139.6
39	-1	1	-1	-1	1	1	72.8
40	1	1	-1	1	1	1	147.8
41	1	-1	1	-1	1	-1	72.7
42	1	1	-1	-1	1	1	80.1
43	1	-1	-1	-1	1	-1	51
44	-1	1	-1	-1	-1	-1	37.2
45	1	1	1	1	1	-1	157.8
46	-1	-1	-1	-1	-1	1	48.8
47	1	1	1	-1	-1	1	84.5
48	1	-1	-1	1	1	1	128
49	-1	1	1	1	1	1	160
50	1	-1	1	-1	-1	-1	53.9
51	1	1	1	1	1	1	180.3
52	-1	-1	-1	1	1	-1	98.3
53	-1	-1	1	-1	-1	1	66.2
54	1	1	1	-1	1	1	112.8
55	-1	-1	-1	1	-1	1	98.7
56	-1	1	1	-1	1	-1	73.5
57	-1	-1	-1	-1	-1	-1	32.5
58	1	-1	-1	1	-1	1	114.6
59	-1	1	1	-1	-1	1	76.2
60	1	-1	1	1	1	1	158.9
61	-1	-1	1	-1	-1	-1	47.9
62	-1	1	-1	1	-1	-1	97.2
63	1	-1	1	-1	-1	1	76.6

64	-1	-1	1	1	1	-1	122.6
65	-1	1	1	1	-1	-1	122.8
66	-1	1	-1	1	-1	-1	98.2

The proxy equation derived from the full factorial design contains seven main terms and thirty-five interacting terms, which give a near perfect fit to the observed volumes. This is a further indication that main terms (linear) alone cannot predict the volume with sufficient accuracy. Including interacting terms can greatly increase the accuracy of the volume equation (Figure 54a). Analysis of the residual plots shows that the volume errors given by the full factorial design are less than $2*10^7$ ft^3 (Figure 54b). This is about 5% of the smallest reservoir volume of ca. $40*10^7$ ft^3 (low case of all parameters) and ca 1% of the largest reservoir volume (high case for all parameters).

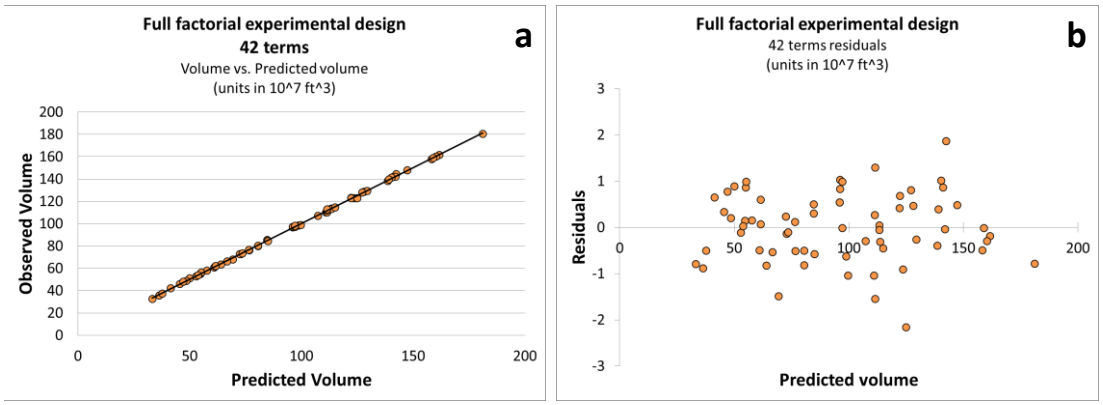

Figure 54. Full factorial experimental design 25 terms. a) Observed volume vs. Predicted volume. b) Residual plot.

Backward elimination optimizes the volume equation to find the best-fit model with fewer terms, and subsequently fewer coefficients to solve. The volume equation takes the form:

$$V_{pred} = \beta_0 + \beta_1 * A + \beta_2 * B + \beta_3 * C + \beta_4 * D + \beta_5 * E + \beta_6 * F + \beta_7 * AD + \beta_8 * BD + \beta_9 * CD + \beta_{10} * AF + \beta_{11} * AC + \beta_{12} * BC + \beta_{13} * BE + \beta_{14} * BF + \beta_{15} * DF + \beta_{16} * EF + \beta_{17} * CE + \beta_{18} * BEF + \beta_{19} * CDE + \beta_{20} * DE + \beta_{21} * CDF + \beta_{22} * EF + \beta_{23} * CEF + \beta_{24} * DEF + \beta_{25} * ABD \quad (4.1)$$

The parameters, coefficients and their meaning are summarized in table 7. By eliminating terms with significance higher than 0,05 derives a volume equation with seven main terms and twenty-five interactions. This volume equation is more practical and retains the same accuracy as the forty-two term equation (Figure 55a). The residual plot of the new equation shows a single outlier, shown by the red circle, and a slightly larger variance (Figure 55b).

Table 7. Explanation of the parameters and coefficients in the 25 term volume equation. Also shown is the significance of each term to the volume equation.

Parameter	**Coefficient**	**Coefficient value**	**Significance**
-	β0	96.14	<0.0001
A - Fault 1	β1	5.927	<0.0001
B - Fault 2	β2	6.569	<0.0001
C - Time horizon	β3	12.55	<0.0001
D - Time thickness	β4	31.36	<0.0001
E - Depth horizon	β5	8.485	<0.0001
F - Depth thickness	β6	9.803	<0.0001
AD	β7	2.444	<0.0001
BD	β8	2.268	<0.0001
CD	β9	1.497	<0.0001
AF	β10	0.815	<0.0001
AC	β11	0.838	<0.0001
BC	β12	0.744	<0.0001
BE	β13	0.713	<0.0001
BF	β14	0.619	0.0001
DF	β15	-1.028	<0.0001
EF	β16	0.972	<0.0001
CE	β17	0.959	<0.0001
BEF	β18	0.3	0.0481

CDE	β19	-0.503	0.002
DE	β20	-0.603	0.0004
CDF	β21	-0.522	0.0015
EF	β22	0.515	0.0019
CEF	β23	0.472	0.0037
DEF	β24	-0.378	0.0179
ABD	β25	0.3	0.0456

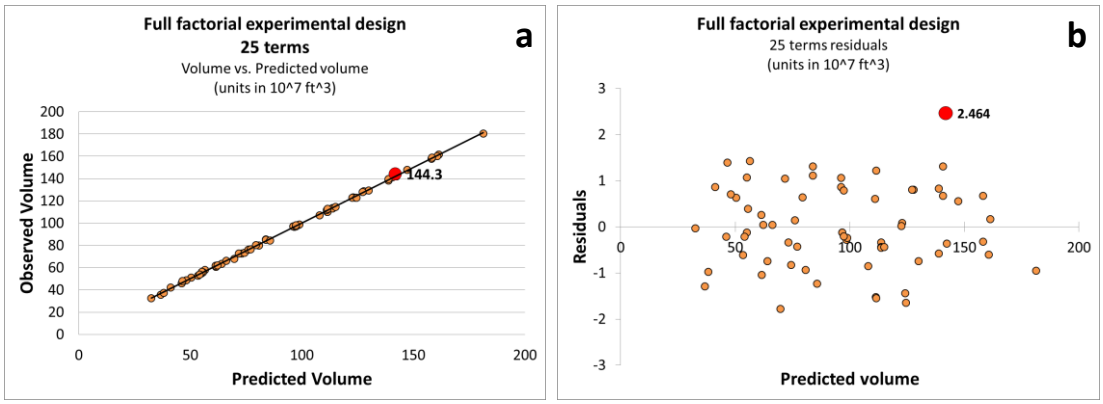

Figure 55. Full factorial experimental design 25 terms. a) Observed volume vs. Predicted volume. b) Residual plot

The uncertainty in the gross-volume is calculated by stochastically changing the parameter values between [-1,1] for five-thousand simulations of the volume equation (Figure 56a). The cumulative density function shows that there is a 90% probability the reservoir volume will be greater than $66*10^7$ ft^3 and 10% probability it will be higher than $123*10^7$ ft^3 (Figure 56b).

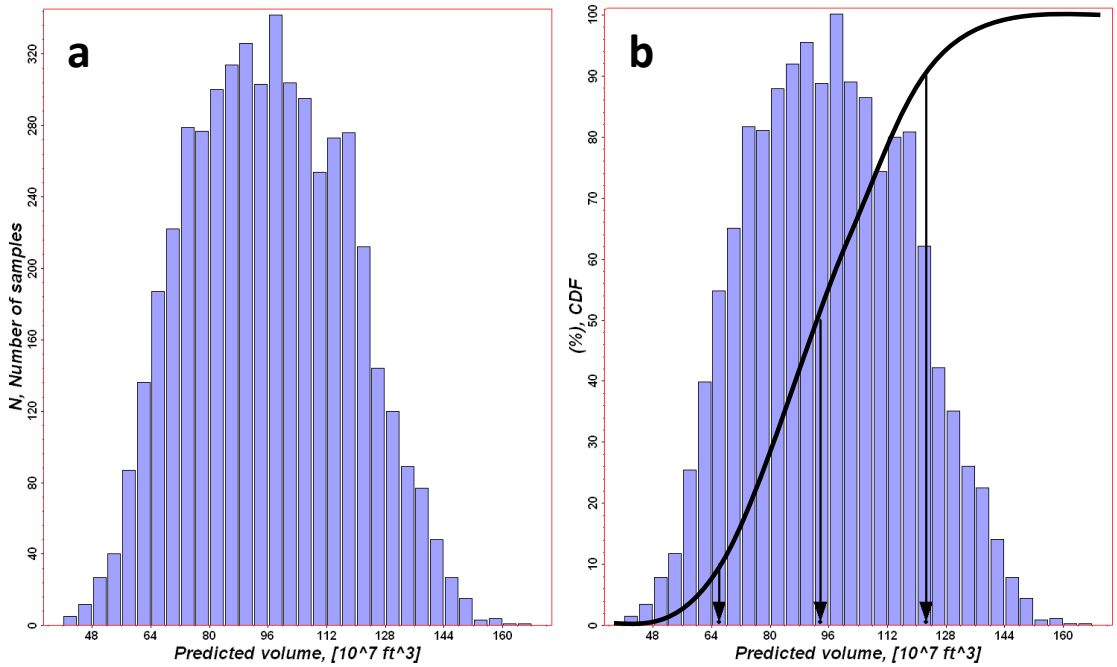

Figure 56. a) Volume distribution for 5000 calculations of the volume equation. b) Cumulative density function of the volume distribution.

4.4.1 Numerical 3-D reservoir model

Sometimes a 3-D model is needed for a specific reservoir volume given by the proxy equation. For instance, the reservoir engineer may request a model referring to a specific volume probability. The following procedure describes how to derive the model parameters for a specific run of the proxy equation in order to build the 3-D model (Table 8).

Table 8. Random experimental run and its corresponding numerical 3-D model.

Volume equation results							
Exp #	**Fault 1**	**Fault 2**	**HorizonT**	**ThicknessT**	**HorizonD**	**ThicknessD**	**Resp_Volume**
1	0.55	0.39	0.94	-0.08	-0.78	0.54	109.2

Numerical 3-D model results							
Exp #	**Fault 1**	**Fault 2**	**HorizonT**	**ThicknessT**	**HorizonD**	**ThicknessD**	**Resp_Volume**
1	0.55	0.39	0.94	-0.08	-0.78	0.54	106.1

All reservoir parameters are described with Gaussian distribution, apart from the faults. Therefore, each parameter value given by the experimental run acts as a weight between ± one standard deviation of the error distributions. For example, the new position for the time horizon is obtained by shifting the top reservoir by:

$$HorizonT = 0.94 * \sigma$$

Where σ represents the standard deviation of the time horizon. The same method is applied to all parameters whose uncertainty is represented by a Gaussian distribution.

The new fault position is obtained by scaling the extreme values [-1,1], used in experimental design, to be represented as values on the interval [0,1], as shown in figure 57. This indicates that a value of 0, 0.5 and 1 on the interval [0,1] represents the low, base and high case fault position, respectively.

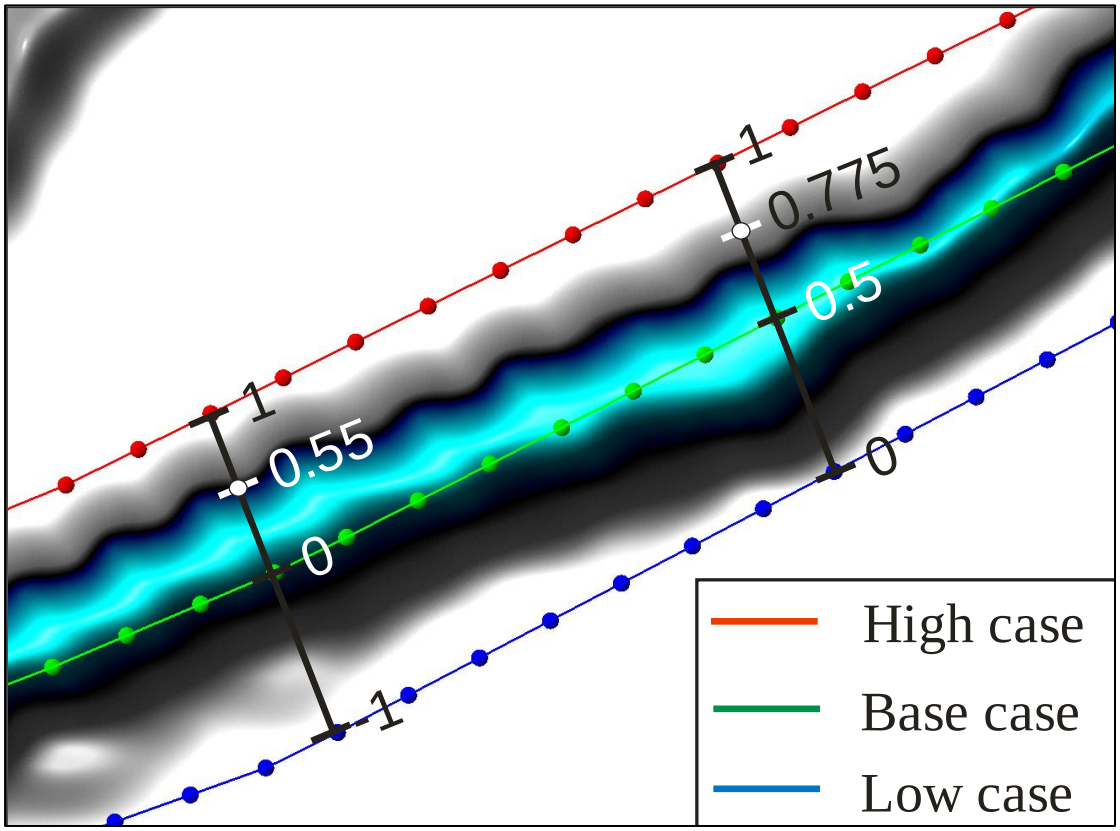

Figure 57. Fault parameter values scaled to the interval [0,1].

The new fault position is calculated by:

$$Fault1_i = 0.775 * d_i$$

Where d_i is the distance between a node "i" on the low case fault polygon and its corresponding node on the high case fault polygon, shown as circles in figure 57.

Figure 58a shows the modeled volume used for calculating the coefficients of the proxy equation versus the predicted volume. The red circle indicates the two volumes linked to the randomly selected model. The red circle on the residual plot in Figure 58b shows that the proxy equation overestimates the volume by about 3%.

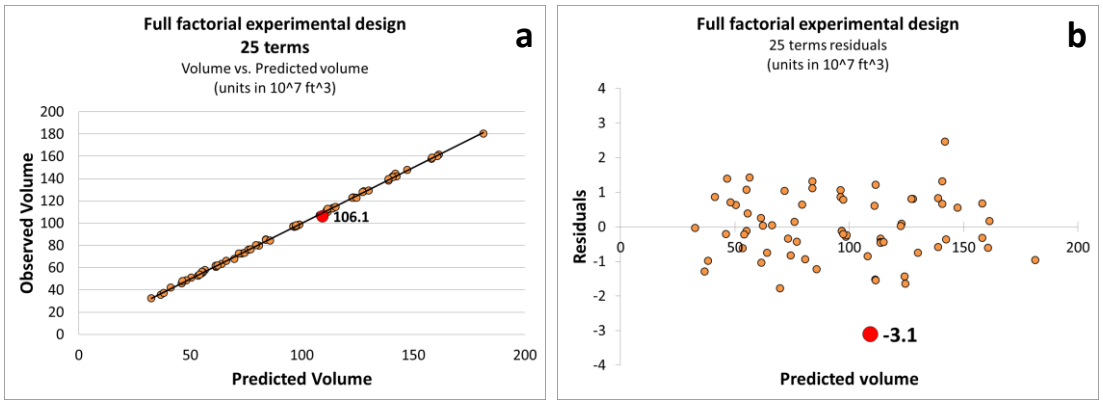

Figure 58. Full factorial experimental design for 25 terms. a) Observed volume vs. predicted volume, numerical model indicated with red circle. b) Residual plot.

5. Discussion

5.1 UNCERTAINTY IN STRATIGRAPHIC HORIZONS

All uncertainties related to stratigraphic horizons in this study are quantitative and represented by a Gaussian distribution. The benefit of using a Gaussian distribution for describing the uncertainties is that if the mean and standard deviation are known, it is possible to compute the percentile rank associated with any given score. In other words, the standard deviation delivers the criteria for deriving the high and low case model parameters.

One source of the seismic uncertainties affecting the stratigraphic horizons is time migration, where seismic events are relocated to the location the event occurred in the subsurface. Time migration is not working accurately in case of strong lateral velocity variations (Hubral *et al.,* 1980). This may be the case for instance due to major velocity boundaries with a steep slope. Another source of uncertainty is static problems, which appear as amplitude variations between traces. At sea, the water is homogeneous and static problems are minimal, unless the ocean floor is irregular (Pritchett, 1990). Structural smoothing solves the static problem. However, this process has the unwanted side effect of smoothing out real properties. This type of uncertainty can be thought of as noise in the natural system. A difference map of the original seismic volume and a smoothed volume shows that uncertainties due to statics have a Gaussian distribution and account for ± 1.32 ms, and therefore their impact is insignificant for the uncertainty study (see Figure 35).

The structural geometries of the reservoir limit the influence of the top reservoir location. The reservoir shows a steep slope and consequently the OWC cuts

the reservoir under a relative steep angle. A considerable part of the reservoir base is above the OWC as well. Therefore, a change of the top reservoir position in time has only a limited effect on the reservoir volume. Separating the uncertainties of the overburden and the reservoir units by stacking thickness maps below the top reservoir allows the analysis of the reservoir thickness uncertainty. For an average thickness of 24 ms, the thickness error standard deviation of 6.5 ms is about 27% of the reservoir thickness. This explains why the reservoir thickness uncertainty has a dominant influence on the reservoir volume uncertainty (see Figure 53).

5.2 UNCERTAINTY IN FAULT POSITION

The influence of the fault uncertainty on the reservoir volume depends on the relationship between the volume covered by the fault zone within the reservoir and the reservoir volume. There is significant subjectivity involved in deriving the envelope of the fault zones. In this thesis, the envelope is described by the high and low case fault positions from interpreted fault polygons on ant tracking time slices. Each polygon set was densely sampled and a new node drawn half the distance between each node on the high and low case fault polygon to represent the base case fault position. A more accurate method would be to define a rotation matrix for the fault object in strike direction and compute the true stratigraphic thickness between the extreme cases. This method more accurately derives the fault geometry while honoring the full extent of the uncertainty envelope defined by the extreme cases.

5.3 UNCERTAINTY IN DEPTH CONVERSION

The choice of gridding algorithm (moving average) interpolates the V_0 to an average value outside the influence radius of the wells; subsequently this method has relatively small deviations of depth errors compared to other gridding methods that use the slope of the data points (see Table 4). The blind well test delivers a standard deviation of 7.84 ft, which is about 0.12% of the average depth. Small deviations in the depth thickness uncertainty are observable. The reservoir thickness depth error distribution delivers a standard deviation of 12.05 ft. This is about 12% of the average thickness. Consequently, its influence on the reservoir volume is not dramatic.

Similarly, as explained in section 5.1, the amount of volume translated above and below the OWC due to depth conversion depends on the structural geometry of the reservoir. This explains why the depth conversion has such a low impact on the reservoir volume for a thin, dipping reservoir. As the result, if the reservoir would not show a significant slope the depth conversion probably has a larger impact where it would be divided horizontally into an oil zone at the top and a water zone at the base.

5.4 EXPERIMENTAL DESIGN

A key benefit of experimental design is that it works with extreme cases of the parameter values, rather than stochastic simulation.

For example, the uncertainty in reservoir thickness can be modelled by stochastically simulating an error surface and adding it to the thickness. A stochastic simulation of an error surface produces many surfaces that have the same properties controlled by a random number generator. The simulation of the error surface depends not only on the standard deviation but also on a couple of simulation parameters, i.e.

the variogram parameters. As these parameters are subject to uncertainty, addressing the uncertainty stochastically becomes complicated. When working with experimental design and low, base and high cases for each parameter the volume uncertainty estimation becomes simpler and easier to quality check. In addition, any combination of parameter values used by the proxy equation is reproducible as a numerical model.

6. Conclusion

Uncertainty is a well-known concept in geology, and can lead to reevaluation of important development decisions if properly assessed. A general method of handling uncertainty is by describing it in the form of a probability density function or a cumulative distribution function.

This thesis provides a robust methodology for capturing the structural uncertainty and its impact on the volumetrics. Key elements of this method are using Gaussian error distributions for defining the low and high case for the reservoir parameters. In addition, a novel method based on volumetric seismic attributes was introduced for capturing the fault uncertainty. Finally, a method was developed that allows to extract the modeling parameters from any parameter setting of the proxy equation describing the reservoir volume. This study has shown that a small variation in a reservoir parameter can mean a significant change in reservoir volume.

The main sources of uncertainty lie within the data source used for structural modeling. The quality of seismic reflection surveys is highly dependent on acquisition and processing. Volume attributes can improve the signal to noise ratio or enhance structural features, where the seismic resolution is an issue, thus making the interpretation more reliable.

One interesting result is that the uncertainties in the seismic picks and consequently in the reservoir thickness have a much greater impact on the gross-volume compared to the influence of faults and velocity uncertainties. The uncertainties in the top reservoir in the time and depth domain have only a moderate influence on the volume uncertainty, which is related to the structural geometries of

the reservoir. The constant interval velocity used for the depth thickness uncertainty is a good approximation of the interval velocities of the reservoir. This indicates that the interval velocities of the reservoir do not change significantly, consequently resulting in minor uncertainty in the depth thickness. The uncertainty of the fault position would also have a greater influence on the volume uncertainty if the reservoir area is small and the fault displacement uncertainty relatively large. This study shows that seismic uncertainties in the reservoir thickness have a larger impact on thin reservoirs.

The limitation of the described method is that it requires a sufficient amount of drilled wells in order to derive meaningful error distributions. Sufficient well data is not always available at the development stage. In addition, different tectonic settings introduce new parameters to the uncertainty analysis, where the reservoir drapes onto a salt dome for instance or along a convergent plate boundary. Thus, a wider range of structurally complex models involving a large number of parameters should be evaluated.

References

Bárdossy, G., & Fodor, J. (2001). Traditional and new ways to handle uncertainty in geology. *Natural Resources Research, 10*(3), 179-187.

Bascle, B. J., Nixon, L. D., & Ross, K. M. (2001). *Atlas of Gulf of Mexico Gas and Oil Sands as of January 1, 1999*: Minerals Management Service, Gulf of Mexico OCS Region, Office of Resource Evaluation.

Bird, D. E., Burke, K., Hall, S. A., & Casey, J. F. (2005). Gulf of Mexico tectonic history: Hotspot tracks, crustal boundaries, and early salt distribution. *AAPG bulletin, 89*(3), 311-328.

Caers, J. (2005). *Petroleum geostatistics*: Richardson, TX: Society of Petroleum Engineers.

Caers, J. (2011). *Modeling uncertainty in the earth sciences*. Chichester: Wiley-Blackwell.

Galloway, W. E. (2008). Depositional evolution of the Gulf of Mexico sedimentary basin. *Sedimentary basins of the world, 5*, 505-549.

Hart, B. S. (2011). Structural Interpretation *An Introduction to Seismic Interpretation* (pp. 42): AAPG.

Hubral, P., Krey, T., & Larner, K. L. (1980). *Interval velocities from seismic reflection time measurements*: Society of Exploration Geophysicists Tulsa.

Lecour, M., Cognot, R., Duvinage, I., Thore, P., & Dulac, J. C. (2001). Modelling of stochastic faults and fault networks in a structural uncertainty study. *Petroleum Geoscience, 7*(4 SPEC. ISS.), 31-42.

Mann, C. J. (1993). Uncertainty in geology. *Computers in Geology–25 Years of Progress, Oxford University Press, Oxford*, 241-254.

Osypov, K., Nichols, D., Woodward, M., Zdraveva, O., Qiao, F., Yarman, E., Ivanova, N. (2011). *From quantifying seismic uncertainty to assessing E&P risks and the value of information.* Paper presented at the 2011 SEG Annual Meeting.

Plackett, R. L., & Burman, J. P. (1946). The design of optimum multifactorial experiments. *Biometrika*, 305-325.

Pritchett, W. C. (1990). *Acquiring better seismic data*: Springer Science & Business Media.

Røe, P., Georgsen, F., & Abrahamsen, P. (2014). An Uncertainty Model for Fault Shape and Location. *Mathematical Geosciences, 46*(8), 957-969.

Samson, P., Dubrule, O., & Euler, N. (1996). *Quantifying the impact of structural uncertainties on gross-rock volume estimates.* Paper presented at the NPF/SPE European 3-D Reservoir Modelling Conference.

Schlumberger, 2009, Petrel manual: Velocity Modeling Course: Schlumberger

Schlumberger, 2010, Petrel manual: Interpreter's Guide to Seismic Attributes: Schlumberger

Srivastava, R. M. (1992). *Reservoir characterization with probability field simulation.* Paper presented at the Proceedings - SPE Annual Technical Conference and Exhibition.

Steppan, D. D., Werner, J., & Yeater, R. (1998). Essential regression and experimental design for chemists and engineers. *MS excel add in software package, 2001*.

Thore, P., Shtuka, A., Lecour, M., Ait-Ettajer, T., & Cognot, R. (2002). Structural uncertainties: Determination, management, and applications. *Geophysics, 67*(3), 840-852.

Vincent, G., Corre, B., & Thore, P. (1999). Managing structural uncertainty in a mature field for optimal well placement. *SPE Reservoir Evaluation and Engineering, 2*(4), 377-384.